Reduced-order unsteady aerodynamic models at low Reynolds numbers

STEVEN L. BRUNTON[1]†, CLARENCE W. ROWLEY[1] AND DAVID R. WILLIAMS[2]

[1]Department of Mechanical and Aerospace Engineering, Princeton University, Princeton, NJ 08544, USA

[2]Department of Mechanical, Materials, and Aerospace Engineering, Illinois Institute of Technology, Chicago, IL 60616, USA

(Received 16 October 2012)

This paper develops reduced-order models for the unsteady lift on a pitching and plunging airfoil over a range of angles of attack. In particular, we analyze the pitching and plunging dynamics for two cases: a two-dimensional flat plate at $Re = 100$ using high-fidelity direct numerical simulations, and a three-dimensional NACA 0006 airfoil at $Re = 65,000$ using wind tunnel measurements. Models are obtained at various angles of attack, and they are verified against measurements using frequency response plots and large amplitude maneuvers. These models provide a low-dimensional balanced representation of the relevant unsteady fluid dynamics. In simulations, flow structures are visualized using finite-time Lyapunov exponents.

A number of phenomenological trends are observed, both in the data and in the models. As the base angle of attack increases, the boundary layer begins to separate, resulting in a decreased quasi-steady lift coefficient slope and a delayed relaxation to steady-state at low frequencies. This extends the low-frequency range of motions that excite unsteady effects, meaning that the quasi-steady approximation is not valid until lower frequencies than are predicted by Theodorsen's classical inviscid model. Additionally, at small angles of attack, the lift coefficient rises to the steady-state value after a step in angle, while at larger angles of attack, the lift coefficient relaxes down to the steady-state after an initially high lift state. Flow visualization indicates that this coincides with the formation and convection of vortices at the leading edge and trailing edge. As the angle of attack approaches the critical angle for vortex shedding, the poles and zeros of the model approach the imaginary axis in the complex plane, and some zeros cross into the right half plane. This has significant implications for active flow control, which are discussed. These trends are observed in both simulations and wind tunnel data.

1. Introduction

The unsteady aerodynamics of small-scale wings at a high angle of attack is at the focus of efforts to study bird and insect flight as well as to develop advanced controllers for high-performance micro air vehicles (MAVs). The short time scales involved in gusts and agile maneuvers make small wings susceptible to unsteady laminar separation, which can either enhance or destroy the lift depending on the specific maneuver. For example, certain insects (Birch & Dickinson 2001; Zbikowski 2002; Sane 2003; Wang 2005) and birds (Videler *et al.* 2004) use the shape and motion of their wings to maintain the high

† Email address for correspondence: sbrunton@princeton.edu

transient lift from a rapid pitch-up, while avoiding stall and the substantially decreased lift that follows. The enhanced performance observed in bio-locomotion relies on unsteady mechanisms that will be important for model-based control of MAVs (Zbikowski 2002; Pines & Bohorquez 2006). The overarching goal of this analysis is to gain an understanding of the underlying unsteady flow physics of pitching and plunging airfoils and to develop tractable reduced-order models suitable for feedback control.

The most important parameter for quantifying the trend towards smaller, slower vehicles is the dimensionless Reynolds number, $Re = cU_\infty/\nu$, where c is the chord length of the wing, U_∞ is the free-stream velocity, and ν is the kinematic fluid viscosity. Small, lightweight vehicles typically experience low Reynolds number, both because of shorter wing chord length and because lighter weight leads to a lower stall velocity. Flow over an airfoil at low Reynolds number is characterized by a thick laminar boundary layer that may have a stable separation bubble for moderate angles of attack. The effect of Reynolds number and aspect ratio on stationary small wings is discussed in Torres & Mueller (2004) and Kaplan *et al.* (2007).

Unsteady aerodynamic forces are readily excited for small vehicles at low Reynolds numbers, in response to either a gust disturbance, aggressive maneuvering, or high-frequency wing motion. The nondimensional parameters governing unsteadiness in the flow over a pitching and plunging rigid airfoil are the Strouhal number and the reduced frequency. The Strouhal number is given by $St = fA/U_\infty$, where f is the frequency of oscillation and A is the peak-to-peak amplitude of the airfoil motion. Triantafyllou *et al.* (1993) and Anderson *et al.* (1998) demonstrated that for a pitching or plunging airfoil, the Strouhal number is typically in the range of 0.25-0.35 for efficient propulsion, although aspect ratio has been shown to play a significant role (Buchholz & Smits 2008; Green & Smits 2008). The reduced frequency, $k = \pi fc/U_\infty$, is frequency non-dimensionalized by chord length. Both nondimensional frequencies increase with higher frequency oscillations and smaller free-stream velocities, and they both decrease with smaller wing size. Reduced frequency unsteadiness is excited by very rapid maneuvers, regardless of amplitude, while Strouhal number unsteadiness is excited by a combination of fast and large motion.

Flight dynamic time-scales are shorter for MAVs than for traditional aircraft, because MAVs are lighter and more compact. Therefore, smaller vehicles are able to perform aggressive maneuvers without the body inertia attenuating the motion, as is the case for large aircraft. As flight dynamic and aerodynamic time-scales become comparable, it is more difficult to simultaneously meet various control objectives. This highlights the need for accurate low-order models that are compatible with both flight dynamic models and with modern, robust feedback control techniques.

Ahuja & Rowley (2010) demonstrated that the flow past a stationary flat plate, with 2% thickness at $Re = 100$, undergoes a supercritical Hopf bifurcation at a critical angle of attack, $\alpha_c \approx 27^\circ$. Above this angle, the flow is characterized by periodic, laminar vortex shedding. They go on to develop feedback controllers, based on balanced proper orthogonal decomposition (BPOD) models (Rowley 2005), to suppress vortex shedding at large angles of attack; their actuation is a localized body force near the trailing edge, and the sensors measure velocity at two locations in the near-wake.

Figure 1 shows the lift coefficient, C_L, against a static angle of attack, α, at the same Reynolds number ($Re = 100$) for a flat plate with 1% thickness; in this case the Hopf bifurcation occurs at $\alpha_c \approx 28^\circ$. If the angle of attack varies in time, the lift coefficient may deviate significantly from the static lift curve, as seen by the sinusoidal pitching and pitch-up, hold, pitch-down maneuvers. The deviation is caused by transient forces, including unsteady viscous effects, which are especially important at low Reynolds numbers, and

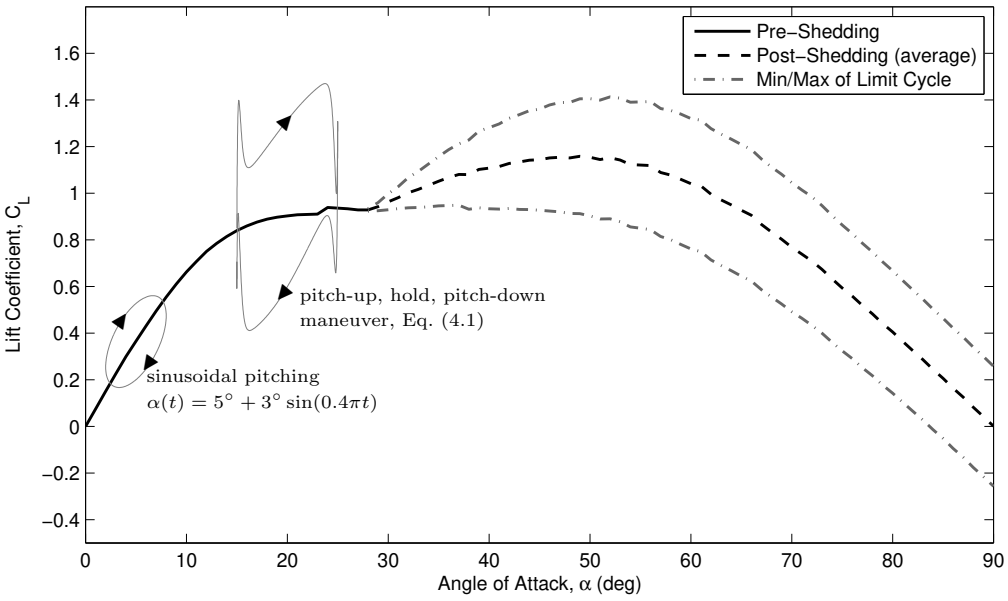

FIGURE 1. Lift coefficient, C_L, against the static angle of attack, α. The flow undergoes a Hopf bifurcation at $\alpha_c \approx 28^\circ$. Unsteady airfoil motion causes deviations from the static lift curve.

large added-mass forces, which are given by the rate-of-work supplied to accelerate fluid out of the way of an accelerating body.

In this work, we build on the ideas in Ahuja & Rowley (2010) by using direct lift measurements and actuating the position of the wing. In keeping with the wind-tunnel perspective, including limited actuator and sensor capability, we do not make use of any linear or adjoint simulations. Instead, we construct maneuvers that are designed to excite linear unsteady phenomena in the full nonlinear system, and obtain reduced-order models using the eigensystem realization algorithm (ERA) of Juang & Pappa (1985). Ma *et al.* (2011) have recently shown that the resulting models are equivalent to BPOD models, but without the need for adjoint simulations.

We develop a reduced-order modelling framework to obtain models for the unsteady aerodynamics of pitching and plunging airfoils at various angles of attack. The models are linearized about a particular flow configuration, determined by the angle of attack, wing shape, and Reynolds number, resulting in a hierarchy of models over a range of parameters. A family of aggressive pseudo-random airfoil maneuvers is devised to identify models from wind tunnel measurements. Special care must be taken, since obtaining large reduced frequencies in a wind tunnel commonly involves decreased flow speeds and subsequently reduced signal-to-noise ratio measurements. The models obtained are low-dimensional, state-space representations that are ideal for use with modern robust and optimal control techniques, which will be particularly important when flight dynamic and aerodynamic time-scales are comparable. Models are developed for $Re = 100$ flow past a two-dimensional flat plate and for $Re = 65,000$ flow past a NACA 0006 airfoil.

The unsteady lift data, and the resulting models, are then used to analyze properties of the unsteady flow field up to large angles of attack. In particular, models are tested over a range of reduced frequencies and angles of attack, including large amplitude, massively separated flows. The numerical results in this paper are visualized using finite-time Lyapunov exponent (FTLE) fields (Haller 2002; Shadden *et al.* 2005). FTLE methods

have been used to study low Reynolds number aquatic propulsion (Peng & Dabiri 2008; Wilson *et al.* 2009; Green *et al.* 2011), as well as 3D turbulence (Green *et al.* 2007) and general vortex phenomena (Franco *et al.* 2007; Shadden *et al.* 2007). Lagrangian methods, such as FTLE, are particularly useful for identifying separated flows (Haller 2004; Surana *et al.* 2006; Weldon *et al.* 2008). In this work, we use FTLE fields to infer lift mechanisms based on unsteady separated flows.

2. Classical unsteady aerodynamic models

The classical models of Theodorsen (1935) and Wagner (1925), and their variants (von Karman & Sears 1938), remain widely used (Pullin & Wang 2004), and they provide inspiration for the state-space models in this paper as well as a benchmark to compare against. Theodorsen's model extends the quasi-steady thin airfoil theory to include added-mass forces and the effect of idealized wake vorticity on the circulation around the airfoil. The model assumes purely harmonic input motion of the angle of attack α and the vertical position h, so that $\alpha(t) = \mathrm{Re}(\tilde{\alpha}(t))$ and $h(t) = \mathrm{Re}(\tilde{h}(t))$, where $\tilde{\alpha}(t) = \bar{\alpha}e^{i\omega t}$ and $\tilde{h}(t) = \bar{h}e^{i\omega t}$, respectively. Defining the lift coefficient $C_L = 2L/\rho U_\infty^2 S$, where L is lift, ρ is the fluid density, U_∞ is the free-stream velocity, and S is the wing area (or the chord for a two-dimensional airfoil), Theodorsen's model is given by $C_L = \mathrm{Re}(\tilde{C}_L)$, where $\tilde{C}_L$ is

$$\tilde{C}_L = \underbrace{\frac{\pi}{2}\left[\ddot{\tilde{h}} + \dot{\tilde{\alpha}} - a\ddot{\tilde{\alpha}}\right]}_{\text{added-mass}} + \underbrace{2\pi\left[\tilde{\alpha} + \dot{\tilde{h}} + \dot{\tilde{\alpha}}\left(\frac{1}{4} - a\right)\right]}_{\text{quasi-steady}} C(k). \tag{2.1}$$

Here, $C(k)$ is the complex-valued Theodorsen's lift deficiency function, describing the attenuation of circulation around the airfoil by previously shed wake vorticity, in terms of the reduced frequency, $k = \omega c/2U_\infty$. Length is nondimensionalized by the chord length c and velocity is nondimensionalized by U_∞, the free-stream velocity. The pitch-axis location a is measured with respect to the 1/2-chord ($a = -1/2$ is the leading-edge, and $a = 1/2$ is the trailing-edge). Extensions of Theodorsen's model have been developed for time-domain analysis of arbitrary maneuvers (Edwards 1977; Brunton & Rowley 2012).

The form of Theodorsen's model, composed of physically motivated terms, is particularly attractive. However, Theodorsen's model is inviscid and assumes infinitesimal motion of the airfoil, resulting in a planar wake. These assumptions are not valid for low Reynolds number flows with thick, laminar boundary layers that may have significant separation and complex wake structures.

Wagner's model is formulated in the time-domain by a convolution integral, and it is functionally equivalent to Theodorsen's model. This is the first of a set of general indicial response models, based on analytic, numerical, or experimental step-response data (Truong & Tobak 1990; Lesieutre *et al.* 1994). A general indicial response model for the circulatory lift in response to an arbitrary pitch motion, $\alpha(t)$, is given by:

$$C_L^{\mathrm{circ}}(t) = \phi(t)\alpha(0^-) + \int_0^t \phi(t-\tau)\dot{\alpha}(\tau)d\tau \tag{2.2}$$

where the "indicial response" $\phi(t)$ is the response of the lift coefficient given a step in the angle of attack. Although this model can be quite accurate, the convolution integral formulation has two major drawbacks: first, the model is not in a state-space form that allows for modern analysis and robust control design, and second, the contributions of various force terms are all lumped into the indicial response ϕ, making parameterization difficult.

The strengths and weaknesses of the above methods motivate the reduced-order models presented in the following section. In particular, we present a framework for obtaining low-dimensional state-space models from either theoretical, numerical, or experimental lift measurements that retain many of the desirable features of the models above.

3. State-space unsteady aerodynamic models

This section presents reduced-order models for the discrete Navier-Stokes equations with moving airfoil boundary conditions and lift force output equation, linearized about an equilibrium state. Model reduction yields low-dimensional, state-space representations of the unsteady lift coefficient, C_L, in response to pitching and plunging airfoil motion. The resulting models are accurate for a specific wing shape, configuration, and Reynolds number, and they may be built from direct numerical simulations or experimental data.

Consider the general, nonlinear unsteady aerodynamic system arising from the unsteady Navier-Stokes equations, written in the general form

$$\begin{aligned} \dot{\boldsymbol{x}}_a &= \boldsymbol{f}(\boldsymbol{x}_a, \boldsymbol{u}; \boldsymbol{\mu}) \\ \boldsymbol{y} &= \boldsymbol{g}(\boldsymbol{x}_a, \boldsymbol{u}; \boldsymbol{\mu}), \end{aligned} \tag{3.1}$$

where $\boldsymbol{x}_a \in \mathbb{R}^n$ contains relevant information about the aerodynamic state (vorticity or velocity field, angle of attack, amount of separation, etc.), $\boldsymbol{u} \in \mathbb{R}^p$ contains the inputs to the system (wing kinematics, actuators, etc.), $\boldsymbol{y} \in \mathbb{R}^q$ are the outputs of interest (forces, moments, pressure, etc.), and $\boldsymbol{\mu} \in \mathbb{R}^k$ are parameters (e.g., Reynolds number). The function $\boldsymbol{f}$ is related to the nonlinear Navier-Stokes equations, for example as the discretized equations from a fluid solver, or the equations resulting from Galerkin projection onto a set of basis functions.

3.1. *Linearized pitch and plunge models*

For a model of the unsteady lift coefficient, C_L, in response to pitching motion, a general state $\boldsymbol{x}_a$ will include the fluid state $\boldsymbol{x}$ (e.g., the vorticity $\boldsymbol{\omega}$ or velocity $\boldsymbol{v}$ at grid points), as well as the angle of attack α, its rate of change $\dot{\alpha}$, and the angular acceleration $\ddot{\alpha}$, resulting in a model of the form

$$\begin{aligned} \dot{\boldsymbol{x}}_a \triangleq \frac{d}{dt}\begin{bmatrix} \boldsymbol{x} \\ \alpha \\ \dot{\alpha} \end{bmatrix} &= \begin{bmatrix} \boldsymbol{f}_{\mathrm{NS}}(\boldsymbol{x}, \alpha, \dot{\alpha}, \ddot{\alpha}) \\ \dot{\alpha} \\ \ddot{\alpha} \end{bmatrix} \\ C_L &= g_{\mathrm{lift}}(\boldsymbol{x}, \alpha, \dot{\alpha}, \ddot{\alpha}) \\ &= g_\nu(\boldsymbol{x}, \alpha, \dot{\alpha}) + g_\phi(\dot{\alpha}, \ddot{\alpha}), \end{aligned} \tag{3.2}$$

where $\boldsymbol{f}_{\mathrm{NS}}$ are the discretized Navier-Stokes equations. The output is split into viscous forces g_ν, and added-mass forces g_ϕ, which depend linearly on $\dot{\alpha}$ and $\ddot{\alpha}$ (Brennen 1982). The input to (3.1) could also be vertical plunging motion $\ddot{h}$ or horizontal surging motion $\ddot{g}$.

Linearizing (3.2) about an equilibrium flow $\bar{\boldsymbol{x}}(\alpha_0)$ at a base angle of attack $\alpha_0 < \alpha_c$ yields a model for the lift coefficient C_L in response to pitch motion $\ddot{\alpha}$:

$$\begin{aligned} \frac{d}{dt}\begin{bmatrix} \boldsymbol{x} \\ \alpha \\ \dot{\alpha} \end{bmatrix} &= \begin{bmatrix} \mathsf{A} & \mathsf{B}_1 & \mathsf{B}_2 \\ \mathsf{0} & 0 & 1 \\ \mathsf{0} & 0 & 0 \end{bmatrix}\begin{bmatrix} \boldsymbol{x} \\ \alpha \\ \dot{\alpha} \end{bmatrix} + \begin{bmatrix} \mathsf{B}_3 \\ 0 \\ 1 \end{bmatrix}\ddot{\alpha} \\ C_L &= \begin{bmatrix} \mathsf{C} & C_\alpha & C_{\dot{\alpha}} \end{bmatrix}\begin{bmatrix} \boldsymbol{x} \\ \alpha \\ \dot{\alpha} \end{bmatrix} + C_{\ddot{\alpha}}\ddot{\alpha}, \end{aligned} \tag{3.3}$$

where $\mathsf{A} = \partial \boldsymbol{f}_{\rm NS}/\partial \boldsymbol{x}$, $\mathsf{B}_1 = \partial \boldsymbol{f}_{\rm NS}/\partial \alpha$, $\mathsf{B}_2 = \partial \boldsymbol{f}_{\rm NS}/\partial \dot{\alpha}$, $\mathsf{B}_3 = \partial \boldsymbol{f}_{\rm NS}/\partial \ddot{\alpha}$, $\mathsf{C} = \partial g_\nu/\partial \boldsymbol{x}$, $C_\alpha = \partial g_\nu/\partial \alpha$, $C_{\dot{\alpha}} = \partial(g_\nu + g_\phi)/\partial \dot{\alpha}$, and $C_{\ddot{\alpha}} = \partial g_\phi/\partial \ddot{\alpha}$. It is important to note that Eq. (3.3) is linearized about an equilibrium flow state $\bar{\boldsymbol{x}}(\alpha_0)$ at a base angle of attack α_0 for pitching about a fixed pitch-axis location a. Theodorsen's lift model has recently been cast into the state-space form (3.3) in Brunton & Rowley (2012).

The model in Eq. (3.3) is in a general form with no assumption made about the fluid state $\boldsymbol{x}$. However, we may assume that the fluid state $\boldsymbol{x}$ represents vorticity and that the flow responds instantaneously to pitch acceleration $\ddot{\alpha}$ with an unsteady (irrotational) potential flow, resulting in the added-mass forces $C_{\dot{\alpha}}\dot{\alpha}$ and $C_{\ddot{\alpha}}\ddot{\alpha}$. Therefore, $\mathsf{B}_3 = \mathsf{0}$, so that $\dot{\alpha}$ is the input to the transient fluid dynamics in $\boldsymbol{x}$. Furthermore, as long as A is invertible, we may further simplify the model by defining a new state variable $\tilde{\boldsymbol{x}} = \boldsymbol{x} + \mathsf{A}^{-1}\mathsf{B}_1\alpha$. Writing $\mathsf{B}_{\dot{\alpha}} = \mathsf{B}_2 + \mathsf{A}^{-1}\mathsf{B}_1$, the model (3.3) then takes the form

$$\begin{aligned} \frac{d}{dt}\begin{bmatrix}\tilde{\boldsymbol{x}}\\ \alpha \\ \dot{\alpha}\end{bmatrix} &= \begin{bmatrix}\mathsf{A} & \mathsf{0} & \mathsf{B}_{\dot{\alpha}} \\ \mathsf{0} & 0 & 1 \\ \mathsf{0} & 0 & 0\end{bmatrix}\begin{bmatrix}\tilde{\boldsymbol{x}}\\ \alpha \\ \dot{\alpha}\end{bmatrix} + \begin{bmatrix}\mathsf{0}\\ 0 \\ 1\end{bmatrix}\ddot{\alpha} \\ C_L &= \begin{bmatrix}\mathsf{C} & C_\alpha & C_{\dot{\alpha}}\end{bmatrix}\begin{bmatrix}\tilde{\boldsymbol{x}}\\ \alpha \\ \dot{\alpha}\end{bmatrix} + C_{\ddot{\alpha}}\ddot{\alpha}. \end{aligned} \tag{3.4}$$

In Eq. (3.4), the wing motion $(\alpha, \dot{\alpha}, \ddot{\alpha})$ enter the transient fluid dynamic state $\tilde{\boldsymbol{x}}$ through the $B_{\dot{\alpha}}$ term. It is possible to write an equivalent model by introducing another change of coordinates, $\tilde{\tilde{\boldsymbol{x}}} = \tilde{\boldsymbol{x}} + \mathsf{A}^{-1}\mathsf{B}_{\dot{\alpha}}\dot{\alpha}$, and $\mathsf{B}_{\ddot{\alpha}} = \mathsf{A}^{-1}B_{\dot{\alpha}}$. The resulting model is

$$\begin{aligned} \frac{d}{dt}\begin{bmatrix}\tilde{\tilde{\boldsymbol{x}}}\\ \alpha \\ \dot{\alpha}\end{bmatrix} &= \begin{bmatrix}\mathsf{A} & \mathsf{0} & \mathsf{0} \\ \mathsf{0} & 0 & 1 \\ \mathsf{0} & 0 & 0\end{bmatrix}\begin{bmatrix}\tilde{\tilde{\boldsymbol{x}}}\\ \alpha \\ \dot{\alpha}\end{bmatrix} + \begin{bmatrix}\mathsf{B}_{\ddot{\alpha}}\\ 0 \\ 1\end{bmatrix}\ddot{\alpha} \\ C_L &= \begin{bmatrix}\mathsf{C} & C_\alpha & C_{\dot{\alpha}} - \mathsf{C}\mathsf{A}^{-1}\mathsf{B}_{\dot{\alpha}}\end{bmatrix}\begin{bmatrix}\tilde{\tilde{\boldsymbol{x}}}\\ \alpha \\ \dot{\alpha}\end{bmatrix} + C_{\ddot{\alpha}}\ddot{\alpha}. \end{aligned} \tag{3.5}$$

We may generalize the above model to include pitch, plunge, or combined pitch and plunge motions. The general model is given by

$$\begin{aligned} \frac{d}{dt}\begin{bmatrix}\boldsymbol{x}\\ \boldsymbol{u} \\ \dot{\boldsymbol{u}}\end{bmatrix} &= \begin{bmatrix}\mathsf{A} & \mathsf{0} & \mathsf{0} \\ \mathsf{0} & \mathsf{0} & \mathsf{I} \\ \mathsf{0} & \mathsf{0} & \mathsf{0}\end{bmatrix}\begin{bmatrix}\boldsymbol{x}\\ \boldsymbol{u} \\ \dot{\boldsymbol{u}}\end{bmatrix} + \begin{bmatrix}\mathsf{B}_{\ddot{\boldsymbol{u}}}\\ \mathsf{0} \\ \mathsf{I}\end{bmatrix}\ddot{\boldsymbol{u}} \\ \boldsymbol{y} &= \begin{bmatrix}\mathsf{C} & \mathsf{C}_{\boldsymbol{u}} & \mathsf{C}_{\dot{\boldsymbol{u}}}\end{bmatrix}\begin{bmatrix}\boldsymbol{x}\\ \boldsymbol{u} \\ \dot{\boldsymbol{u}}\end{bmatrix} + \mathsf{C}_{\ddot{\boldsymbol{u}}}\ddot{\boldsymbol{u}}. \end{aligned} \tag{3.6}$$

For this paper, we use a lift coefficient output, $\boldsymbol{y} = C_L$. Pure pitch is given by $\boldsymbol{u} = \alpha$, pure plunge is given by $\boldsymbol{u} = h$, and combined pitch and plunge is given by $\boldsymbol{u} = \begin{bmatrix}\alpha & h\end{bmatrix}^T$.

3.2. *Reduced-order model identification*

Similar to Theodorsen's expression, the models above are written in terms of the quasi-steady and added-mass forces, given by the coefficients $C_{\boldsymbol{u}}, C_{\dot{\boldsymbol{u}}}, C_{\ddot{\boldsymbol{u}}}$ in (3.6), and a model for the transient fluid dynamics, given by $(\mathsf{A}, \mathsf{B}_{\dot{\alpha}}, \mathsf{C})$ in (3.4) and $(\mathsf{A}, \mathsf{B}_{\ddot{\boldsymbol{u}}}, \mathsf{C})$ in (3.6). All of the terms in the models above depend on the specific wing geometry, configuration and Reynolds number used to determine the equilibrium flow state about which the equations are linearized. In both cases, the transient fluid dynamic models are written in terms of

the vector $\boldsymbol{x} \in \mathbb{R}^n$, which is a representation of the fluid state, for example the velocity or vorticity at each grid point; typically, the dimension n is quite large.

We seek a reduced-order model, $(\mathsf{A}_r, \mathsf{B}_r, \mathsf{C}_r)$, of the full-state model, $(\mathsf{A}, \mathsf{B}, \mathsf{C})$, in terms of a low-dimensional state, $\boldsymbol{x}_r \in \mathbb{R}^r$, where $r \ll n$. This reduced-order model is obtained by first identifying and removing the coefficients $C_{\boldsymbol{u}}, C_{\dot{\boldsymbol{u}}}, C_{\ddot{\boldsymbol{u}}}$ from an impulse response in either $\dot{\boldsymbol{u}}$ or $\ddot{\boldsymbol{u}}$, and identifying the remaining transient dynamics using the eigensystem realization algorithm (ERA) of Juang & Pappa (1985). Ma *et al.* (2011) demonstrated that the resulting model captures the r most observable and controllable fluid states in a balanced representation, which is particularly good for efficiently and faithfully representing the input-output relationship for a particular choice of sensors and actuators. Identifying the quasi-steady and added-mass coefficients up-front guarantees accuracy of the model in the limit of low-frequency and high-frequency motions. The modelling effort is then targeted at the transient unsteady fluid dynamics that occurs at intermediate frequencies, allowing for a low-order model that is accurate over a range of frequencies.

The reduced-order models presented in this work are obtained from an approximation of the discrete-time impulse response in either $\dot{\alpha}$ (step in α), $\ddot{\alpha}$ (step in $\dot{\alpha}$), or $\ddot{h}$ (step in vertical velocity). These responses are obtained from maneuvers related to the canonical *pitch-up, hold, pitch-down* maneuver that was developed by Eldredge *et al.* (2009) to study low Reynolds number separation phenomena across simulations and experiments. In the case of direct simulations, a smoothed linear ramp-step is used. This maneuver is ideal for identifying unsteady aerodynamic models, because the unsteady contribution from the quasi-steady, added-mass, and transient terms are separated in time.

For wind tunnel measurements, we use a frequency-rich input maneuver in conjunction with the observer/Kalman filter identification (OKID) algorithm (Juang *et al.* 1991), which estimates the impulse response of a linear system in the presence of noisy measurements. Obtaining high reduced frequencies in a wind tunnel typically involves low free-stream flow velocity, and corresponding low signal-to-noise ratio measurements. Therefore, a pseudo-random sequence of smoothed ramp-steps are concatenated to form an aggressive system identification maneuver. This idea is inspired by the pulsed-blowing identification of Kerstens *et al.* (2011). Because the input to this maneuver is a sequence of discrete impulses in $\ddot{\boldsymbol{u}}$, the model identified is of the form in Eq. (3.6).

After obtaining a discrete-time step response in either $\boldsymbol{u}$ or $\dot{\boldsymbol{u}}$, the quasi-steady and added-mass coefficients $C_{\boldsymbol{u}}, C_{\dot{\boldsymbol{u}}}$, and $C_{\ddot{\boldsymbol{u}}}$ are identified and subtracted from the measured response. Next, a model for the remaining transient fluid dynamics is obtained using the ERA. The transient portion $(\mathsf{A}, \mathsf{B}, \mathsf{C})$ of the model in Eqs. (3.4) and (3.6) is approximated by the ERA model $(\mathsf{A}_r, \mathsf{B}_r, \mathsf{C}_r)$ of order $r \ll n = \dim(\mathsf{A})$; the input is either $\dot{\boldsymbol{u}}$ or $\ddot{\boldsymbol{u}}$ (for example, $\boldsymbol{u} = \alpha$ for pitch), and the output is C_L. The general procedure is summarized:

(a) Obtain the impulse response in either $\dot{\boldsymbol{u}}$ or $\ddot{\boldsymbol{u}}$, possibly via OKID.

(b) Determine $C_{\boldsymbol{u}}$, $C_{\dot{\boldsymbol{u}}}$, and $C_{\ddot{\boldsymbol{u}}}$. The coefficients $C_{\boldsymbol{u}}$ and $C_{\ddot{\boldsymbol{u}}}$ guarantee correct low-frequency and high-frequency behaviour of the model, respectively.

(c) Identify reduced-order model for remaining dynamics with the ERA.

Specific details about the algorithms and maneuvers are provided in Brunton (2012).

4. Results: two-dimensional flow past a flat plate at $\boldsymbol{Re} = 100$

4.1. *Direct numerical simulations*

The numerical results in this paper are based on direct numerical simulations (DNS) of the incompressible two-dimensional Navier-Stokes (NS) equations. We use the fast multi-domain immersed boundary projection method (IBPM) of Taira & Colonius (2007) and

Colonius & Taira (2008). This method has been rigorously verified against standard examples, as well as a low Reynolds number tow-tank experiment in oil (Colonius & Taira 2008).

The immersed body is a rigid flat plate airfoil that may either pitch or plunge with velocity $\boldsymbol{v}_B$. The boundary conditions are uniform flow in the far field, which is valid for a sufficiently large domain, and specified velocity $\boldsymbol{v}_B$ at points along the body. An efficient multi-domain approach is used, resulting in a series of nested grids, each twice as large as the previous. The Poisson equation is solved on the largest domain with zero boundary conditions, and the interpolated stream function from this larger grid is used for the boundary condition on the next smaller grid. The Poisson equation is then solved on this smaller grid, and the process is repeated, until the equations have been solved on all grids. Time integration is performed using the implicit Crank-Nicolson scheme for the viscous diffusion and a third order Runge-Kutta scheme for the convective terms.

The computational domain consists of five nested grids, using the multi-domain approach above. The finest grid covers a domain of 4×4 (with lengths nondimensionalized by chord), and the coarsest covers a domain of 64×64. Each grid has resolution of 400×400, which is sufficient for converged results at $Re = 100$. Additionally, the method is slightly modified to solve the equations of motion in the body-fixed frame of the flat plate by introducing a moving baseflow with uniform and purely rotational components. In this formulation, the locations of the boundary points relative to the grid do not change in time, so that the matrix involved in solving for the boundary forces is constant, and can be decomposed (e.g., by a Cholesky factorization) once at the beginning of the calculation. This approach is significantly faster than available alternatives when the boundary points move relative to the grid.

4.2. *Lagrangian particle analysis*

The finite-time Lyapunov exponent (FTLE) field is used to visualize the unsteady flow field, because it is well suited for identifying regions of separated flow and wake structures. Ridges of the FTLE field that satisfy an additional hyperbolicity condition are Lagrangian coherent structures (LCS) (Haller 2002; Shadden *et al.* 2005), and they are time-varying analogs of the stable and unstable manifolds from dynamical systems theory.

This analysis involves advecting passive tracer particles through the time-varying fluid velocity field by numerical integration, resulting in a particle flow map. The FTLE is the maximum singular value of the flow map Jacobian, logarithmically scaled with respect to the advection time. We use a computationally efficient method to compute the FTLE field (Brunton & Rowley 2010), whereby a flow map with long advection time is broken up into the composition of a number of intermediate flow maps with short advection time. Neighboring FTLE field computations may re-use the intermediate flow maps, which dramatically improves computational efficiency. The FTLE visualizations in this paper are obtained by integrating particles backward in time, yielding FTLE ridges that attract particles in forward time.

Figure 2 shows the attracting FTLE structures for simulated flow past a flat plate at $Re = 100$ in various configurations. Ridges in the FTLE field indicate the stable separated flow behind a stationary plate at $\alpha_0 = 25°$, the vortex shedding behind a stationary plate at $\alpha_0 = 35°$, the von Kármán vortex street behind a pitching plate, and the formation of a large leading-edge vortex for a plunging plate with $\alpha_0 = 20°$ bias.

4.3. *Models linearized at* $\alpha_0 = 0°$

At zero angle of attack, ramped step-response simulations are obtained for a flat plate pitching about various points (leading edge, quarter chord, and middle chord) and plung-

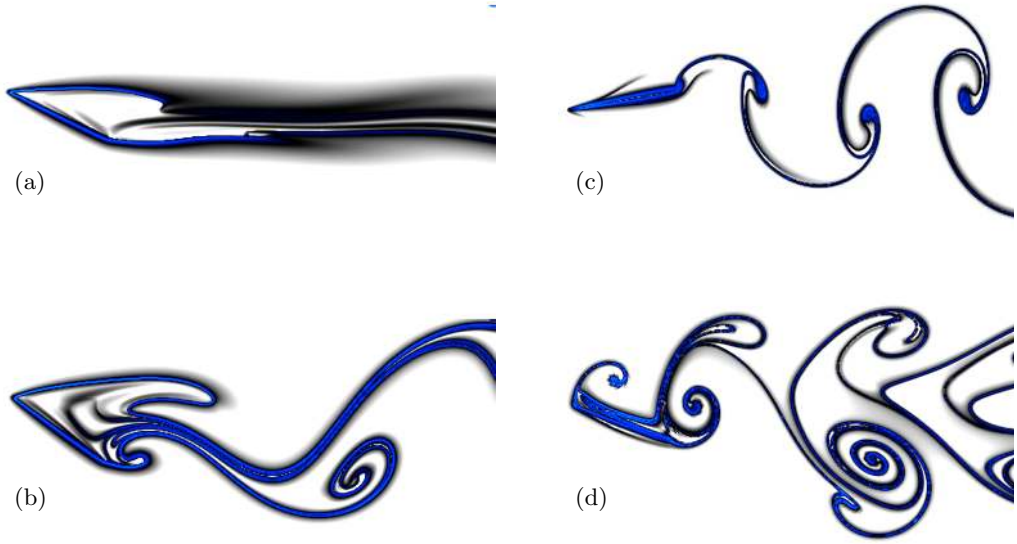

FIGURE 2. Finite-time Lyapunov exponent (FTLE) field for various two-dimensional separated flows. (a) Steady flow past a flat plate at $\alpha = 25°$, (b) Unsteady vortex shedding past a flat plate at $\alpha = 35°$, (c) von Kàrmàn vortex street behind a pitching plate, (d) leading-edge separation for a plunging plate with $\alpha = 20°$. The Reynolds number for all flows is $Re = 100$, and the reduced frequency is $k = 1.26$ for the pitching and plunging cases.

ing vertically. The lift coefficient history from the step-response simulations are synthesized into models of the form in Eq. (3.4) for pitch and Eq. (3.6) for plunge, with ERA models $(\mathsf{A}_r, \mathsf{B}_r, \mathsf{C}_r)$ for the transient viscous fluid dynamics of order $r = 7$. Additionally, a multiple-input model of the form in Eq. (3.6) is obtained that combines plunging with pitching about various points. For the multiple-input case of combined pitch and plunge, the ERA model also has order $r = 7$.

4.3.1. *Small amplitude motions*

The reduced-order models presented are based on ramped step-response simulations with a small step magnitude M; $M = 0.1°$ in the case of pitching motion, and $M = 0.1°$ effective angle of attack ($\dot{h} = 0.00175$) in the case of plunging motion. Therefore, it is natural to compare the models with DNS for small amplitude motions. The frequency response for each model is computed for sinusoidal input $u(t) = M\sin(\omega t)$ with $M = 1°$ for pitch ($u = \alpha$), and $M = 0.01$ for plunge ($u = h$). The input to the models is $\ddot{u} = -M\omega^2\sin(\omega t)$, so that the Bode plot is a frequency response from input $\ddot{u}$ to C_L.

Figure 3 shows the frequency response (i.e. Bode plot) comparing the DNS, reduced-order models (3.4) and (3.6), Theodorsen's model (2.1), and indicial response (2.2) for pitching about the quarter-chord. Similar agreement is found in Bode plots for pitch about the leading-edge and mid-chord as well as for plunge motion. In all of the Bode plots and step-response plots, the low-order ERA models (single-input, single-output as well as the multi-input, single-output) accurately reproduce the frequency response computed by direct numerical simulations. Moreover, the ERA model is nearly identical to the indicial response model, as they are both based on the same numerical step response. Theodorsen's model consistently over predicts the quasi-steady lift slope, and is not as accurate in capturing the phase.

It is important to gain a physical intuition for the Bode plots and how they relate to the aerodynamic response. The low-frequency asymptote in each Bode plot corresponds

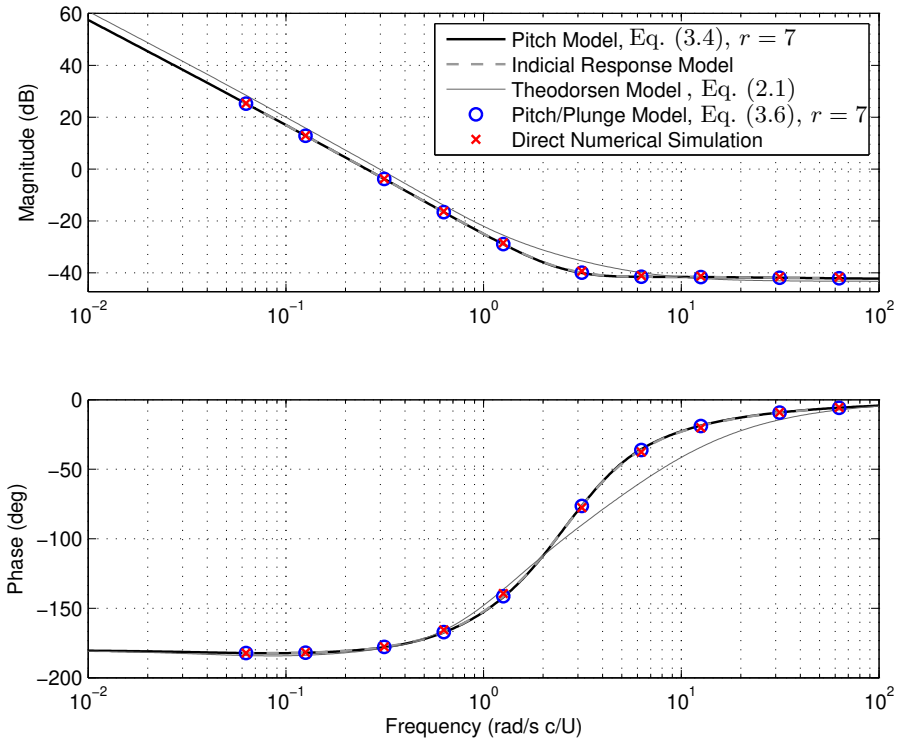

FIGURE 3. Frequency response of reduced-order model (3.4) (7-mode ERA component), indicial response, Theodorsen and DNS (×) for pitching at quarter chord. Multiple-input ERA model (3.6) for pitch/plunge agrees well (circle, ○).

to the quasi-steady case when the lift coefficient depends only on the angle of attack in the case of pitch, or effective angle of attack in the case of plunge. For pitching motion, the low-frequency asymptote in the magnitude plot has a slope of −40 dB/decade†, consistent with the fact that α is obtained by integrating the input $\ddot{\alpha}$ twice. In the case of plunge, the low-frequency asymptote has a slope of −20 dB/decade, since the effective angle of attack is related to $\dot{h}$ which is the integral of the input $\ddot{h}$. In all instances, the low-frequency asymptote of the model is lower than that of Theodorsen's model, which uses the inviscid 2π lift slope and over-predicts the true lift slope at Re= 100. The high-frequency asymptote in the Bode magnitude plot corresponds to the case when there are large accelerations and the lift coefficient is strongly influenced by added-mass forces. In the case of pitch about the quarter-chord and plunge motion, there are added-mass forces directly proportional to the inputs ($\ddot{\alpha}$ and $\ddot{h}$), so that the Bode plot has zero slope at high frequencies. These forces are captured by the $C_{\ddot{\alpha}}$ and $C_{\ddot{h}}$ terms in Eqs. (3.6) and (3.4). There is no added-mass lift force proportional to $\ddot{\alpha}$ in the case of mid-chord pitching, but there are forces proportional to $\dot{\alpha}$, so the Bode plot has a slope of −20 dB/decade at high frequencies. This information is also reflected in the Bode phase plot. The phase at low-frequency starts at −180° for the pitching models, which is consistent with the fact

† A decade is defined as an order of magnitude in frequency, and each integral of the input adds −20 dB/decade to the magnitude slope.

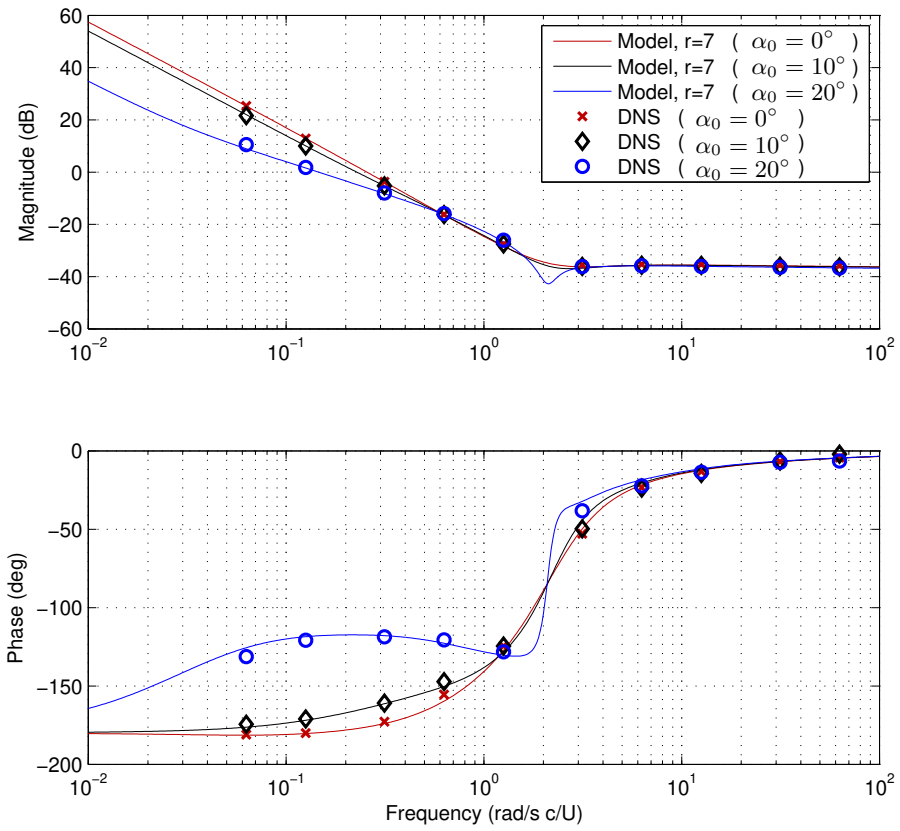

FIGURE 4. Frequency response of models for pure pitching about the leading-edge, linearized at $\alpha_0 = 0°$, $\alpha_0 = 10°$, and $\alpha_0 = 20°$. Results from direct numerical simulation linearized at $\alpha_0 = 0°$, $\alpha_0 = 10°$, and $\alpha_0 = 20°$ are included for comparison.

that the angle of attack is the second integral of the input (twice integrating a sinusoid results in a negative sinusoid, hence the $-180°$ phase).

4.4. *Models linearized at sub-critical angles, $\alpha < \alpha_c$*

As the plate's angle of attack is increased, the flow physics becomes significantly more involved. Increasing the angle of attack results in an adverse pressure gradient on the upper surface that thickens the upper boundary layer until the flow reverses, resulting in a stable, attached separation bubble. Above a critical angle of attack, $\alpha_c \approx 28°$, the separation bubble bursts, resulting in periodic, laminar vortex shedding.

This section presents models for a flat plate linearized at various angles of attack up to the critical angle, α_c, at which a Hopf bifurcation occurs. These cases provide a more challenging demonstration of the modelling procedure, because the transient fluid dynamic interactions are increasingly complex and important at larger angles of attack.

4.4.1. *Frequency domain analysis*

Using the reduced-order modelling technique described in Section 3, we have computed reduced-order models linearized at $\alpha_0 \in [0°, 27°]$ in $1°$ increments. Figure 4 shows the

frequency response of models linearized at $\alpha_0 = 0°$, $\alpha_0 = 10°$, and $\alpha_0 = 20°$, and the corresponding data from DNS. As seen in Figure 1, the lift slope decreases for increasing angle of attack, so it is not surprising that the low-frequency magnitude in the Bode plot decreases for increasing angle of attack. Additionally, we see that at larger angle of attack the phase converges to $-180°$ at lower frequencies, indicating that solutions take longer to reach equilibrium in the time domain. This is consistent with the fact that for larger angles of attack the system is closer to instability, and a pair of eigenvalues of the system approach the imaginary axis, lengthening the time-scale of relaxation.

To see this more clearly, we plot the poles and zeros of the models for $\alpha_0 \in [0°, 27°]$, shown in Figure 5. The model given by Eq. (3.4) always has two poles at the origin because the input $\ddot{\alpha}$ must be integrated twice to obtain the states $\dot{\alpha}$ and α. Because we use an ERA model of order $r = 7$ for the transient dynamics, there are seven branches of poles, in addition to the two poles at the origin; there are nine branches of zeros.

The most striking feature of Figure 5 is that as angle of attack increases, a pair of poles and a pair of zeros march towards the imaginary axis. This explains the longer relaxation times (convergence of Bode plots to $-180°$ at successively lower frequencies). It also indicates that the models are capturing the dynamics as the system approaches a Hopf bifurcation. It is also interesting to note that there is a second set of poles and zeros that branch from the real axis and march toward the imaginary axis for increasing angle of attack. This is consistent with the fact that at larger angle of attack, there is more complicated limit cycle behaviour. It is not surprising that the flow may undergo several Hopf bifurcations as angle of attack or Reynolds number is increased, as observed by Ruelle & Takens (1971).

4.4.2. *Time domain analysis*

The step-response simulations for the various base angles from $\alpha_0 = 0°$ to $\alpha_0 = 27°$ are plotted in Figure 6. The lift coefficient at the base angle is subtracted, and we only plot the transient dynamics after the step, so added-mass is omitted. Notice that between one and five convective times, there is a dip in the lift coefficient followed by a rise to steady state. A 7-mode ERA model is required to capture this feature accurately at all angles, even at $\alpha_0 = 0°$. Interestingly, a 7-mode model is also required to accurately capture the frequency and decay rate of the oscillations in the large angle of attack cases. It is worth noting that this data is based on a small, fast maneuver which yields relatively small variations in the lift coefficient. Although this works well for DNS, the lift variations are hundreds of times smaller than those of a *canonical* maneuver, shown in Figure 7, and they may be too subtle for experimental measurements, motivating the aggressive maneuvers used in the wind tunnel analysis.

A large amplitude pitch-up, hold, pitch-down maneuver, developed by Eldredge *et al.* (2009) to study separation phenomena in pitching airfoils, is given by the following:

$$\alpha(t) = \alpha_0 + \alpha_{\max} \frac{G(t)}{\max(G(t))}, \qquad G(t) = \log\left[\frac{\cosh(a(t-t_1))\cosh(a(t-t_4))}{\cosh(a(t-t_2))\cosh(a(t-t_3))}\right] \tag{4.1}$$

The maneuver from Eq. (4.1) is used, at an angle of attack starting at $\alpha_0 = 15°$ and reaching a maximum angle of 25°; the pitch point is the leading edge, the parameter $a = 11$ determines how sharp the corners are in the maneuver, and $t_1 = 1, t_2 = 3, t_3 = 4, t_4 = 6$. This maneuver excites leading edge separation, as seen in the accompanying FTLE images. The comparison of various reduced-order models with DNS is shown in Figure 7. Theodorsen's model is included for a baseline comparison. The pitch model linearized about $\alpha_0 = 15°$ matches the DNS very closely. The model linearized about $\alpha_0 = 0°$ is more accurate than Theodorsen's model, but has the wrong lift coefficient

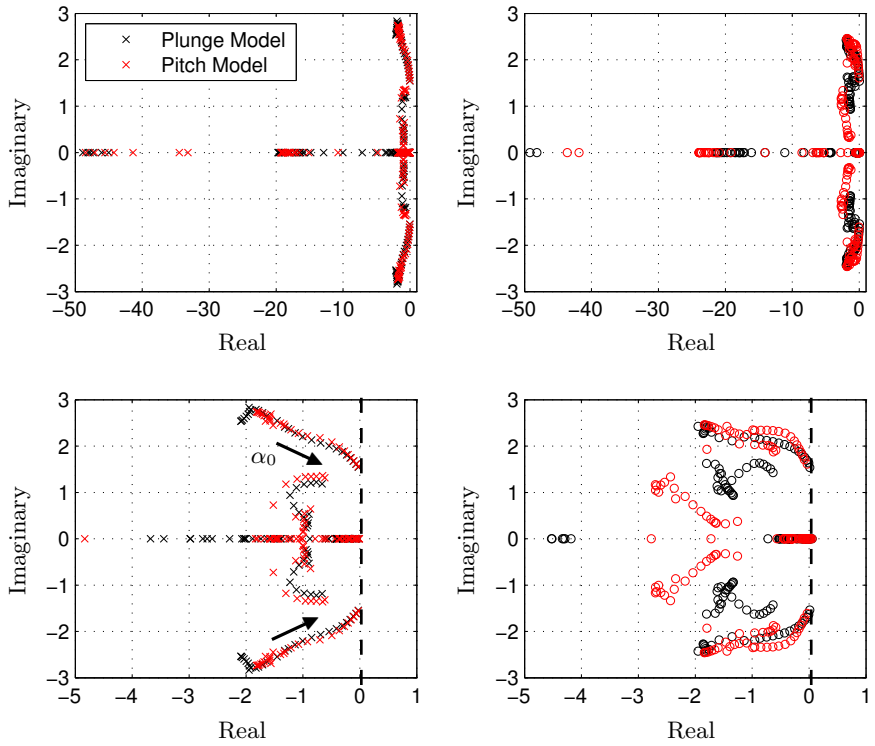

FIGURE 5. Poles (left, ×) and zeros (right, ○) of models for pitch about the middle-chord and plunge, linearized at various angle of attack, from $\alpha = 0°$ to $\alpha = 27°$. (bottom) zoom in.

slope. The $\alpha_0 = 15°$ model is also able to capture the negative slope of the lift coefficient during the constant angle *hold* period between $\tau = 3$ and $\tau = 4$; this is an important feature that is observed at large angles of attack, both in simulations and in experiments.

4.5. *Behavior at post-critical angles,* $\alpha > \alpha_c$

It is important to establish how the linear models from Section 3 perform on large amplitude maneuvers with significant flow separation. For this reason, we consider a number of large amplitude pitch and plunge maneuvers and investigate both the model performance and the flow field itself.

First, consider the pitch-up, hold, pitch-down maneuver from 0° to 45° and back down, given by Eq. (4.1) and shown in the top of Figure 8. This maneuver exceeds the critical angle of attack, and as is seen in the FTLE visualization, a large leading-edge vortex forms and convects downstream. The curve labelled "Hybrid Model" is obtained by running two models, one linearized at $\alpha_0 = 0°$ and another at $\alpha_0 = 25°$, and switching between the models at time $\tau = 3.0$ and again at $\tau = 4.0$. The model does surprisingly well, considering the large separated flow structures, although there is error during each phase of the maneuver. Again, we notice that the slope of the lift response is negative during the hold region. Investigating the FTLE field, we see that the FTLE ridge is parallel to the trailing edge at $\tau = 3.0$, and the ridge moves upstream along the upper surface of the airfoil at $\tau = 4.0$. The trailing edge separation likely accounts for the decreased lift,

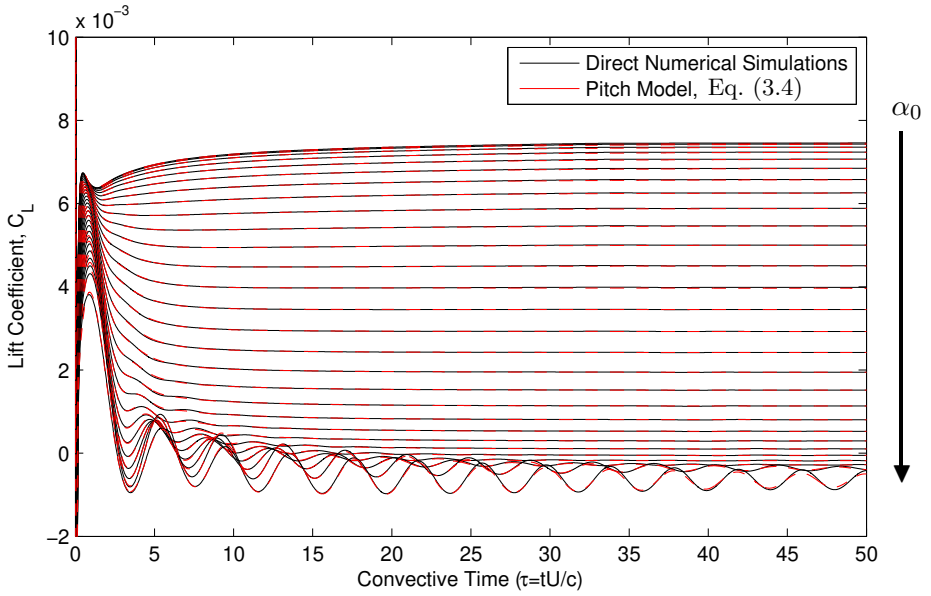

FIGURE 6. Simulations and model prediction for small step in pitch angle about the leading-edge of magnitude $M = 0.1^\circ$ from a reference angle α_0 to $\alpha_0 + M$ for $\alpha_0 \in [0^\circ, 27^\circ]$. The initial lift coefficient $C_L(\alpha_0)$ is subtracted, and α_0 increases with the arrow. ERA model order is $r = 7$.

despite the leading edge vortex that typically provides enhanced lift (Taira & Colonius 2009).

This effect is more pronounced in Figure 9, which shows a flat plate in a sigmoidal pitch-up maneuver to $\alpha = 32^\circ$ at $Re = 300$. Because the airfoil does not pitch back down to $\alpha = 0^\circ$, it is possible to see the free evolution of the leading-edge vortex. Again, there is a clear difference in the high-lift and low-lift states corresponding to whether or not there is trailing edge separation. Because this flow is at a different Reynolds number, and our linear models are not built to capture the nonlinear vortex shedding, we do not include a model comparison.

Finally, we consider an aggressive sigmoidal plunge maneuver in Figure 10. The maximum plunging velocity corresponds to an effective angle of attack of over 40°, based on the formula $\alpha_e = \tan^{-1}(\dot{h}/U_\infty)$; however, this large effective angle of attack is short lived. The reduced-order model, linearized at $\alpha_0 = 0^\circ$ captures the lift coefficient quite well. Again, the FTLE field indicates large leading and trailing edge separation that convect downstream. The majority of the forces throughout the maneuver are added-mass forces, which appear as a doublet in the lift coefficient, which contributes to the good model performance.

4.6. *Summary of numerical results*

Pitch and plunge models have been developed for a flat plate at $Re = 100$ over a range of sub-critical angles of attack, based on data from direct numerical simulations. These models outperform Theodorsen's classical model for all motions investigated, and the performance gap widens at larger base angle of attack, as the flow becomes more separated, and the assumptions of an inviscid, planar wake become less accurate.

A number of interesting flow phenomena arise at large base angles of attack. First, as a pair of model eigenvalues moves towards the imaginary axis, the time-scale for

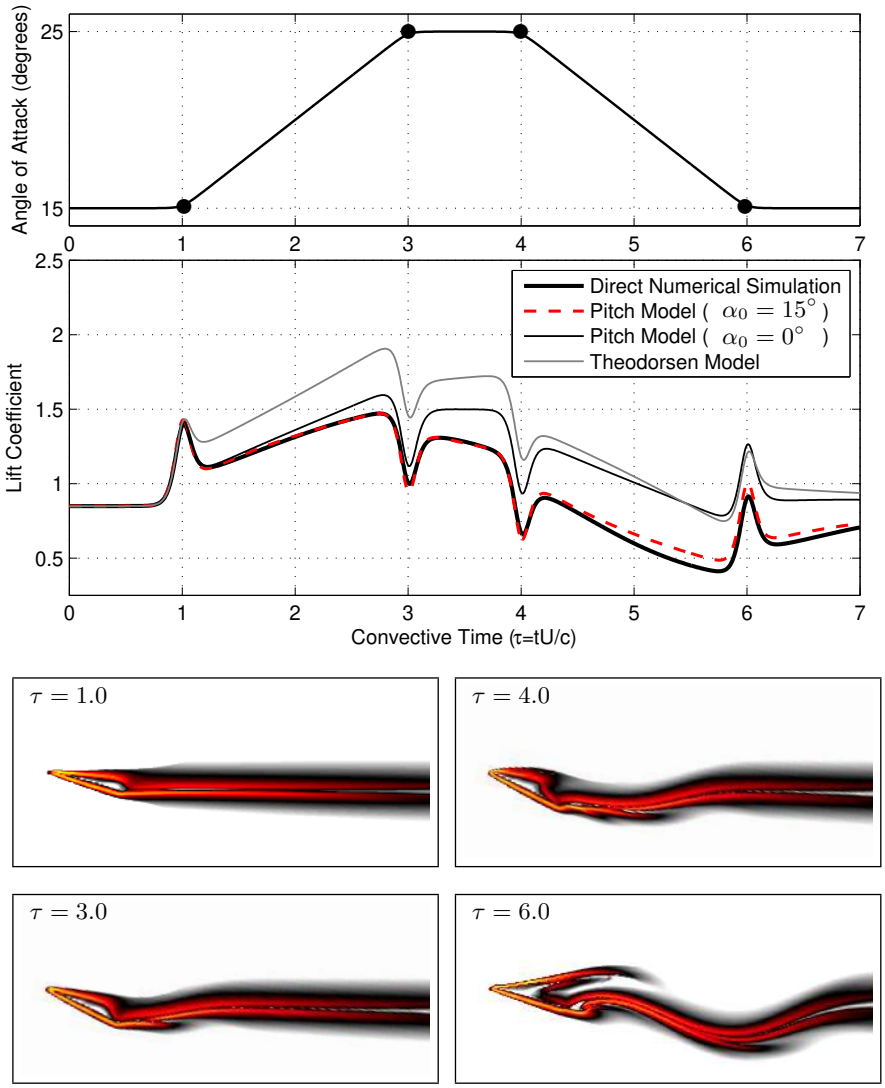

FIGURE 7. Figure showing improved performance of models linearized at $\alpha_0 = 15^\circ$ over models linearized at $\alpha_0 = 0^\circ$ for a pitch maneuver from 15° to 25° and back.

relaxation to steady-state becomes longer. In addition, at a small base angle, the lift rises to a steady-state value after a step in the angle, and at large base angle, the lift starts at an initially high lift and decreases to steady-state. The FTLE fields indicate that the flows have large separation for these maneuvers, and the lift is strongly correlated to the trailing-edge separation condition. Large lift corresponds to streamlined trailing edge flow parallel to the plate, and low-lift states have trailing edge separation, indicated by an FTLE ridge that moves upstream, perpendicular to the plate. The extent of the motion of the trailing-edge separation point upstream is roughly linear in the maneuver, so the model captures the behavior of rapid maneuvers past the critical bifurcation angle.

In the next section, the reduced-order models, Eqs. (3.4) and (3.6), and Theodorsen's model are tested at higher Reynolds numbers in wind-tunnel experiments. Instead of

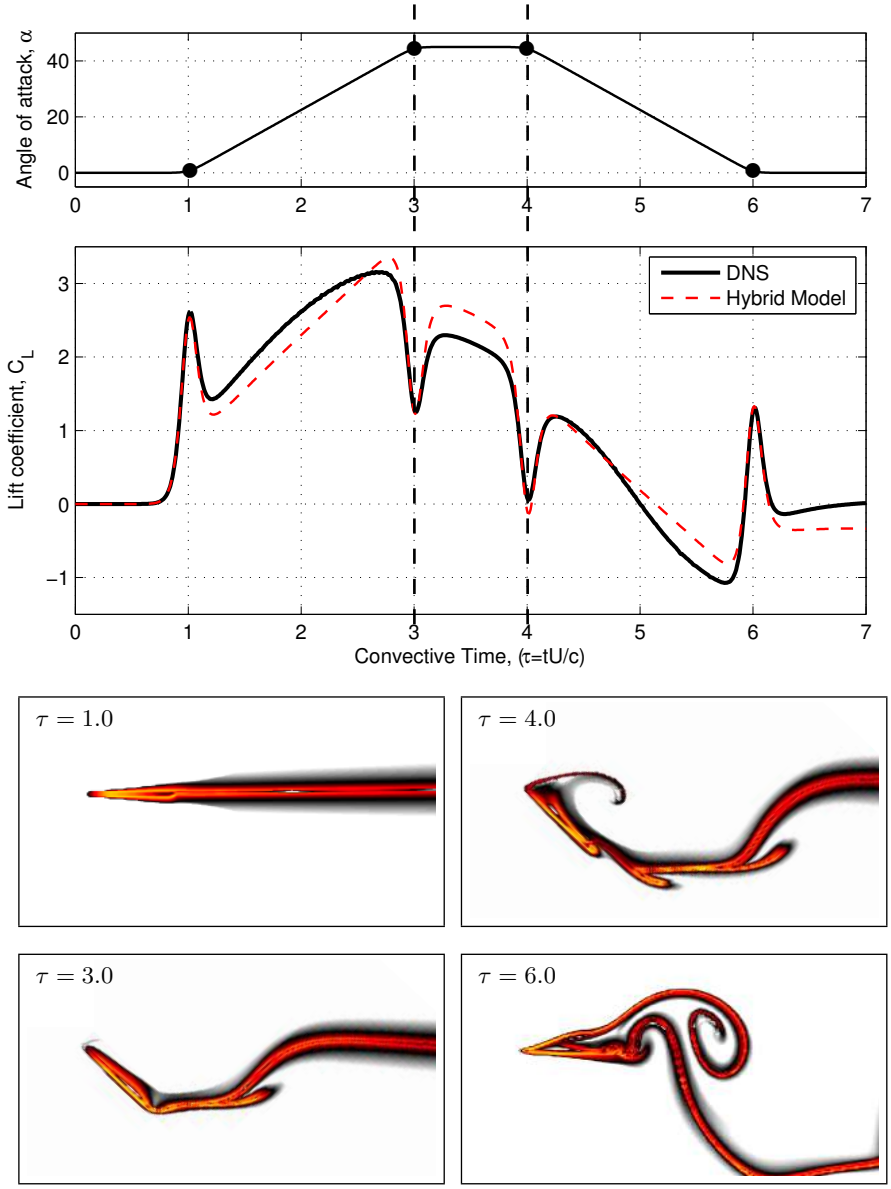

FIGURE 8. Comparison of reduced-order model and direct numerical simulation for large amplitude pitch-up, hold, pitch-down maneuver with a maximum angle of attack of 45°.

a two-dimensional flat plate, we now use a lightweight, three-dimensional NACA 0006 airfoil with rounded leading edge; three-dimensional effects are reduced by having the airfoil span nearly the entire width of the wind-tunnel. The following experimental results at higher Reynolds number are a more realistic test of these models.

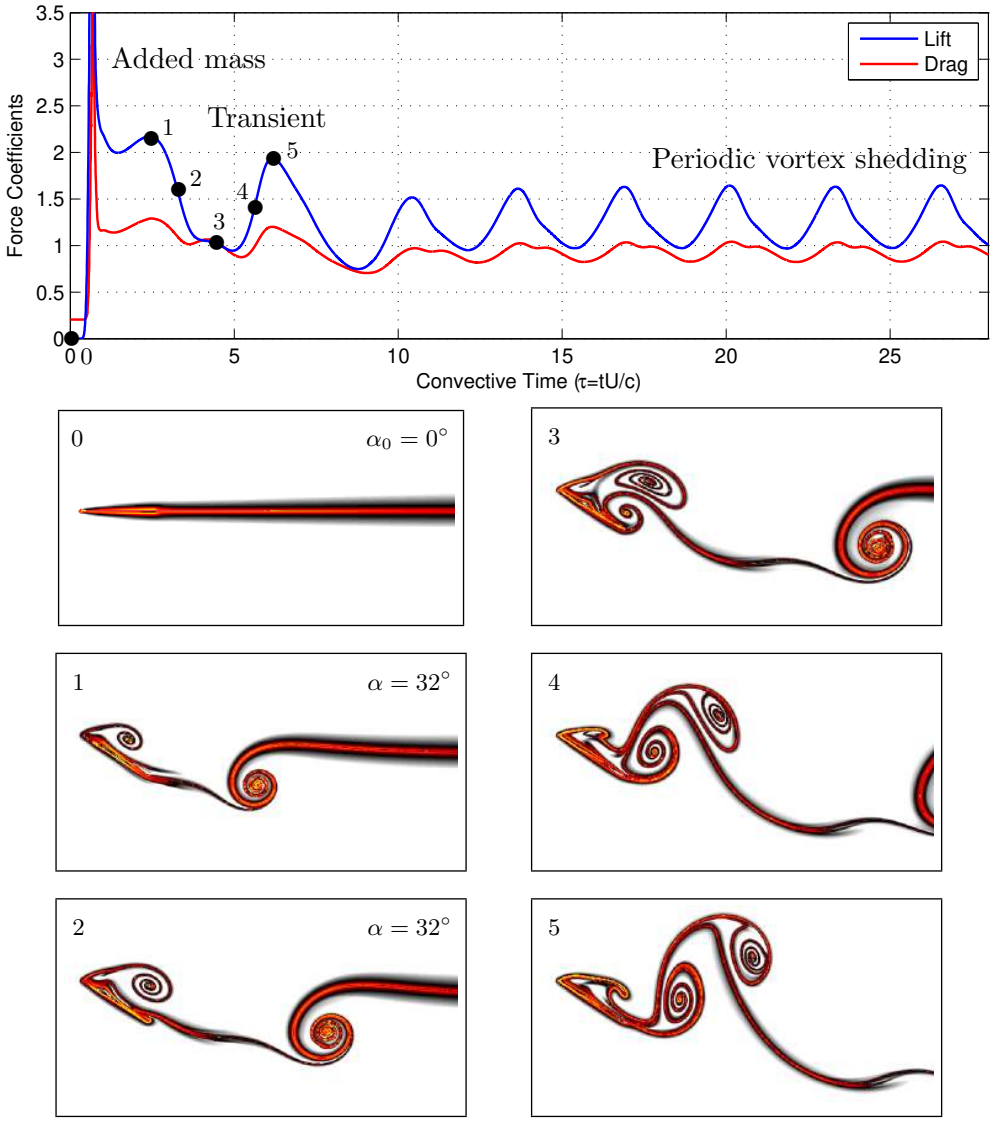

FIGURE 9. Flat plate airfoil in sigmoidal pitch-up about the mid-chord from $\alpha_0 = 0°$ to $\alpha = 32°$ ($Re = 300$). Peaks in lift coefficient (1,5) correspond to streamlined trailing edge condition. Minima of lift coefficient (3) correspond to a trailing edge separation point moving up towards the mid-chord of the airfoil and strong trailing-edge roll-up.

5. Experimental apparatus

The following experimental data was collected in the Andrew Fejer Unsteady Flow Wind Tunnel at the Illinois Institute of Technology. The dimensions of the wind tunnel test section are 0.6m × 0.6m × 3.5m.

The model is a NACA 0006 airfoil, shown in Figure 11 (a), with a chord length of 0.246 m and span of 0.598 m. The free-stream velocity is 4.00 m/s, which results in a Reynolds number of approximately 65, 000 and a convective time of 0.0615 seconds. In all pitching experiments the pitch point is at the 11% chord location.

Forces and moments are measured using a 6-axis ATI Nano17 force transducer. The

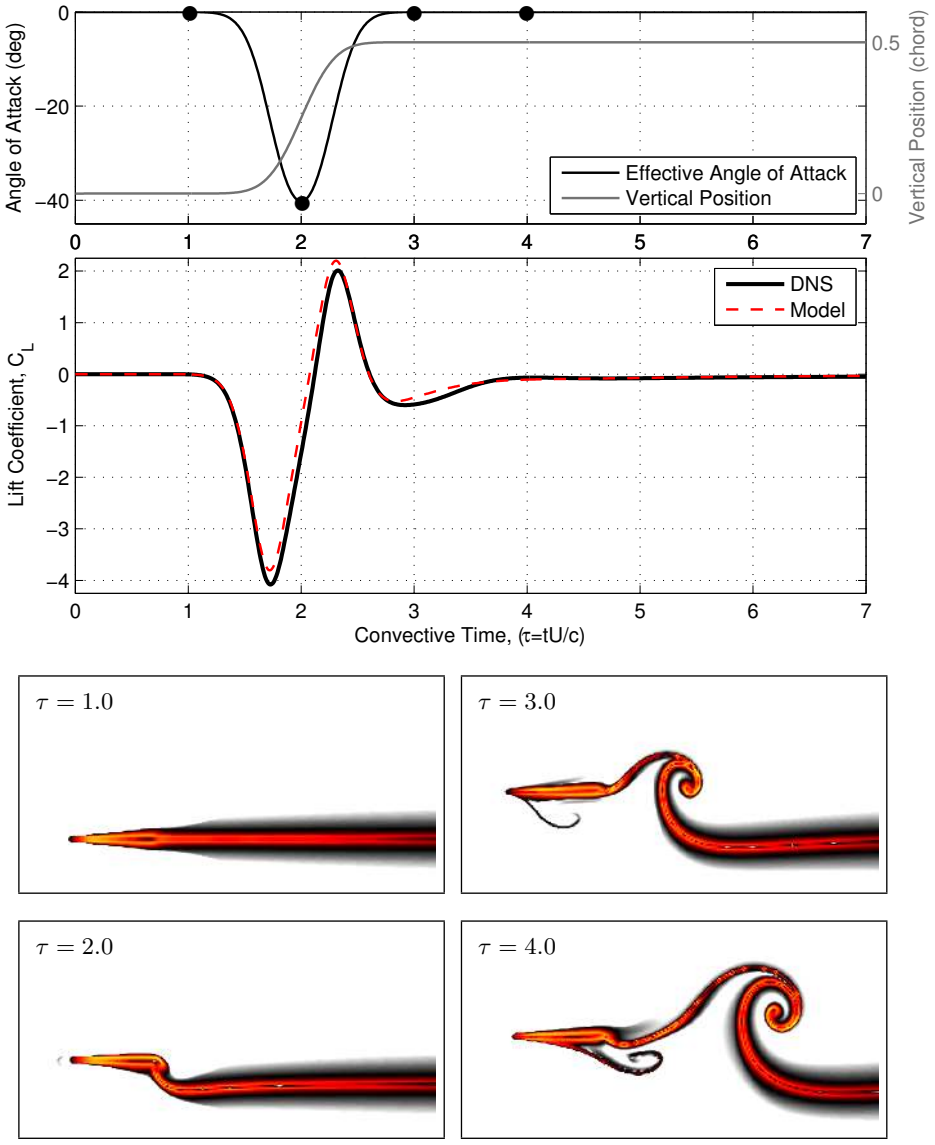

FIGURE 10. Comparison of reduced-order model and direct numerical simulation for sigmoidal plunge maneuver. Even though there are large separated structures, and an effective angle of attack of 40°, the model agrees closely because of the large added-mass forces.

free-stream velocity is measured using a Pitot tube with a Validyne DP-103 pressure transducer. The model is actuated using two Copley servo tubes connected to individual pushrods, allowing for a full range of pitch and plunge motions.

The force transducer moves with the body, so forces are measured in the body-fixed frame of the airfoil. Therefore, we rotate the normal (N) and parallel (P) forces in the z- and x- directions into the lift (L) and drag (D) forces relative to the free-stream velocity:

$$\begin{bmatrix} L \\ D \end{bmatrix} = \begin{bmatrix} \cos(\alpha) & -\sin(\alpha) \\ \sin(\alpha) & \cos(\alpha) \end{bmatrix} \begin{bmatrix} N \\ P \end{bmatrix} \tag{5.1}$$

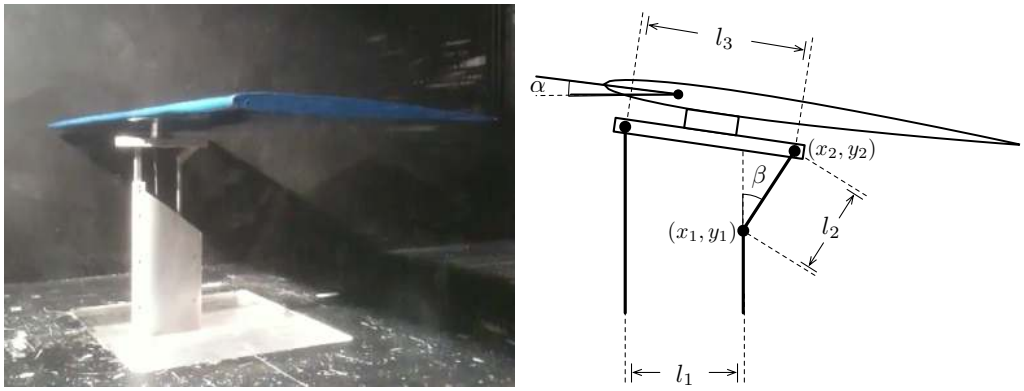

(a) (b)

FIGURE 11. (a) NACA 0006 model in wind tunnel. (b) Schematic of hinge apparatus connecting pushrods to platform.

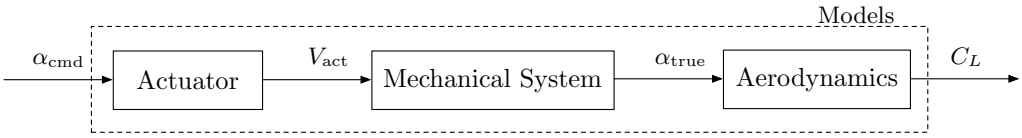

FIGURE 12. Schematic of signals in wind tunnel experiment. V_{act} is the actuator voltage.

The lift and drag forces are then converted into nondimensional force coefficients.

The pushrods are connected to the airfoil and force balance via a lightweight aluminum platform with a hinge constraint, as shown in Figure 11 (b). It is possible to command an angle of attack α by varying the relative displacement of the two pushrods. For the pitching experiments below, the front pushrod is held fixed, and the height of the rear pushrod y_1 is varied to change α. The vertical displacement y_1 may be solved for as a function of α, and vice versa, using the following relationship:

$$(l_3 \cos(\alpha) - l_1)^2 + (-l_3 \sin(\alpha) - y_1)^2 - l_2^2 = 0 \tag{5.2}$$

where $l_1 = 2.1$", $l_2 = 1.25$", and $l_3 = 3$" for the setup in Figure 11.

Finally, the inertia of the model, sting and pushrods introduces time lags, so the measured angle is not exactly the same as the commanded angle. Additionally, the Copley servo tube controller has its own PID dynamics to track a reference position. Figure 12 is a schematic of the signals. The model input is the commanded angle of attack, α_{cmnd}, so that the models include the effect of the actuator and the mechanical apparatus.

5.1. *Phase Averaged Force Measurements*

To reduce the magnitude of sensor noise in the force measurements, we phase average over a number of cycles. Data is collected for N identical runs and averaged, resulting in a reduction of noise by a factor $\sqrt{N}$. The top of Figure 13 shows the force measurements with sensor noise for a 5° step, and the bottom shows the phase-averaged force.

Before phase averaging, we use a 6-th order Butterworth low-pass filter at 2500 Hz. In addition, we coarsen the data by averaging the measurements inside each interval $[k\Delta t, (k+1)\Delta t)$, where $\Delta t = 0.1$ convective time unit, or 0.00615 seconds. Using this coarsened data as an input to the OKID method results in a discrete-time model with

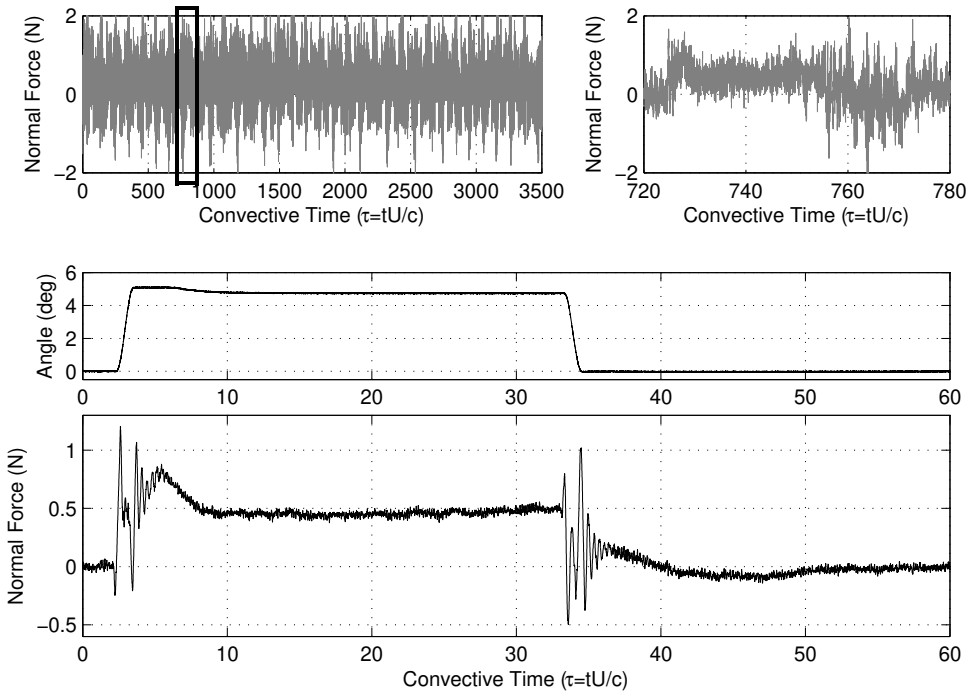

FIGURE 13. Phase-averaged force measurement for 5 degree step-up, step-down.

time-step Δt. Because the high-frequency forces are dominated by added-mass, a time-step of $\Delta t = 0.1$ is sufficiently small to excite and characterize the transient dynamics.

5.2. *Mechanical resonance*

Figure 14 shows the power spectrum of the normal force measurement for a number of experiments designed to isolate the source and frequency of various mechanical resonances. In one case, the bottom of the actuator assembly is struck with a rubber mallet, resulting in a strong resonance at 77 Hz and at 138 Hz. When power is fed to the servo motor controller, a significant resonant peak at 38 Hz develops, regardless of whether or not the wind tunnel fan is on. It is likely that the resonance peak at 38 Hz is a result of the internal PID dynamics of the servo motor controller, partially explaining the peaks in the Bode plots at nearby frequencies in the following section.

6. Results: flow past a NACA0006 airfoil at $\boldsymbol{Re} = 65,000$

Unsteady aerodynamic models are developed for a NACA 0006 airfoil at Reynolds number 65,000 based on wind tunnel measurements discussed in the previous section. Pitch and plunge models of the form in Eq. (3.6) are constructed using the ERA/OKID method in conjunction with aggressive system identification maneuvers described in Section 3. It is shown that the low-order models identified from experiments are more accurate than Theodorsen's model for all maneuvers, especially those based at larger angle of attack. We compute the reduced-order models using an on-design pseudo-random maneuver and test the performance of the models on several pseudo-random off-design maneuvers; the model performance is similar to the on-design case, and these plots are not shown.

After identifying significant mechanical ringing and aeroelastic effects in earlier results,

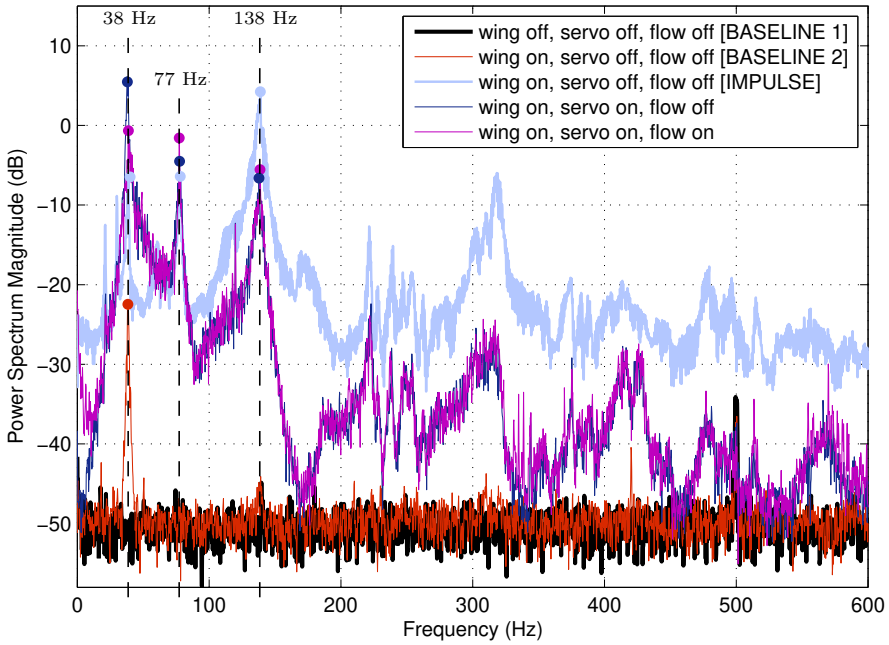

FIGURE 14. Mechanical resonances involved in the wind tunnel experiment. Circles show the relative magnitudes and frequencies of the peaks of each experiment.

the structural supports were rebuilt and the PID controller was tuned to reduce sources of noise and vibration. In addition, a more sensitive Nano17 force transducer is used to measure forces, so that less aggressive maneuvers may be accurately measured.

6.1. *Pitching experiments*

An aggressive pseudo-random maneuver, shown in the top of Figure 15, is used to obtain a reduced-order model of the form in Eq. (3.6) for pitching motion linearized about $\alpha_0 = 0°$. The middle of Figure 15 shows the measured and modeled response. Both models, Eq. (3.6) and Theodorsen's model, appear to closely match the measured force; however, from Table 1 in Section 6.3, Theodorsen's model has nearly twice the error as the ERA model. The agreement with Theodorsen's model at $\alpha_0 = 0°$ speaks to the accuracy of the experiments after mechanical resonances were isolated and removed.

Figure 16 shows the same pitch maneuver performed at a base angle of $\alpha_0 = 10°$. For this maneuver, Theodorsen's model is significantly less accurate than in the $\alpha_0 = 0°$ case. This is not entirely surprising, considering that the flow physics is increasingly complex for larger angles of attack. In addition, the behavior in the *hold* regions is qualitatively different from the $\alpha_0 = 0°$ case: instead of a transient rise to the steady-state value, the lift starts at an initially high value at the beginning of the hold, and decreases to the steady-state value. Similar behavior was observed in simulations, where the difference in behavior was explained by leading-edge and trailing-edge separation, as in Figure 7.

Figure 17 compares the Bode plots of the ERA models at $\alpha_0 = 0°$ and $\alpha_0 = 10°$ and Theodorsen's model. The model linearized at $\alpha_0 = 10°$ converges to the low-frequency asymptote at a lower frequency than the $\alpha_0 = 0°$ model, and the magnitude is smaller at low frequencies, consistent with a decreased lift coefficient slope. Additionally, since

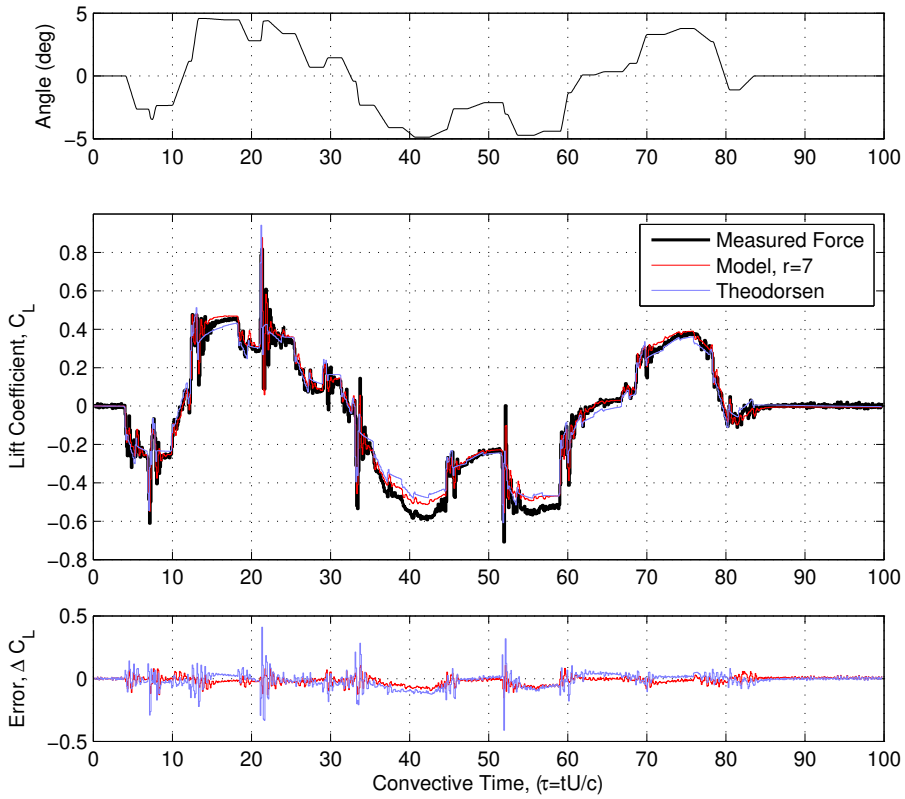

FIGURE 15. Experimental and modeled lift for pitch about a base angle $\alpha_0 = 0°$.

these models include the effect of the actuator and mechanical system, there is a strong mechanical resonance at 30 rad/s c/U, which corresponds to about 76 Hz. The model at $\alpha_0 = 10°$ does not have a prominent resonance at 11 rad/s c/U (28 Hz), unlike the model based at $\alpha_0 = 0°$. It appears that the boundary layer separation at $\alpha_0 = 10°$ has almost entirely eliminated this resonance.

6.2. *Plunge experiments*

An aggressive plunge maneuver can be seen at the top of Figure 18. Since the C_h term is zero in the plunge model (3.6), it is unnecessary to have the *hold* portions of the maneuver at different heights. Therefore, the new maneuver accelerates into linear ramps of different vertical velocity until a maximum or minimum height has been reached, after which the position is held for a time and then the direction is reversed. The different vertical velocities correspond to different *effective* angles of attack.

Figure 18 shows the results for plunging at $\alpha_0 = 0°$ and Figure 19 shows the results for plunging about $\alpha_0 = 10°$. At $\alpha_0 = 0°$ Theodorsen's model is quite accurate, capturing the qualitative behaviour. At $\alpha_0 = 10°$, however, Theodorsen's model fails to predict the regions of constant vertical velocity, which correspond to a constant effective angle of attack. In fact, during these effective angle of attack holds, Theodorsen's model rises to a steady state that is larger in magnitude, while the actual lift decreases from a large initial

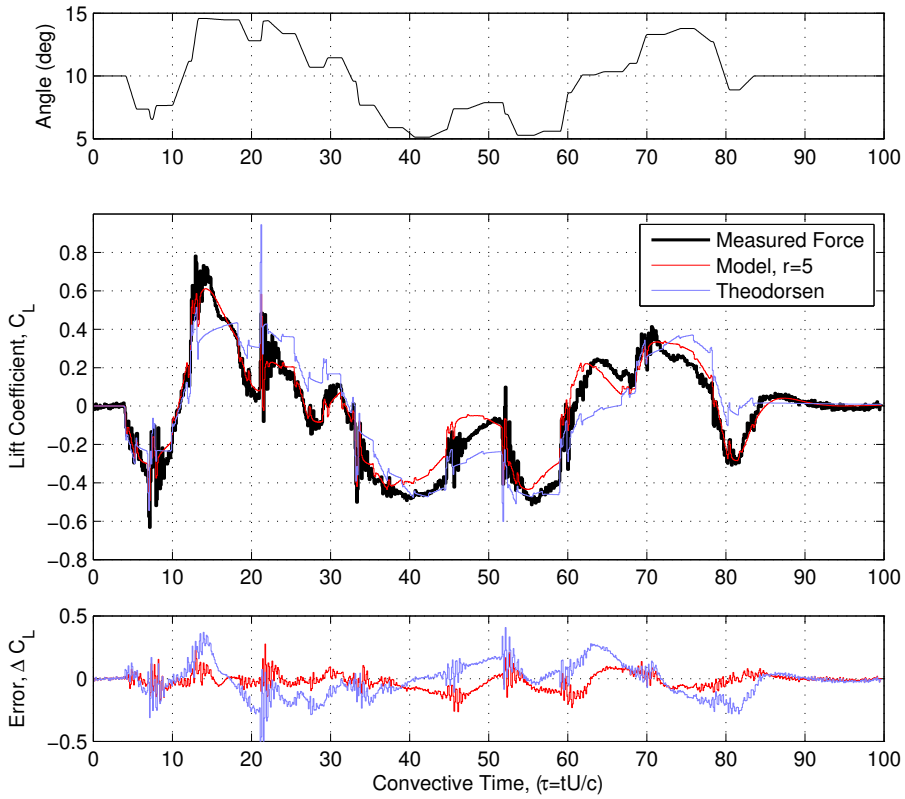

FIGURE 16. Experimental and modeled lift for pitch about a base angle $\alpha_0 = 10^\circ$.

value. Although the reduced-order model is more accurate at capturing this phenomena, it is clear from the error signal that both models systematically underpredict the lift at the beginning of these hold periods.

6.3. *Model benchmarks*

The results of Sections 6.1 and 6.2 are summarized here. Table 1 shows the error between the measured data and both Theodorsen's model and the identified model, Eq. (3.6) from ERA/OKID. The error is measured by integrating the square of the difference between each model and the measured data for a given maneuver. In each case, the error in the ERA model is about half of the error in Theodorsen's model. The error increases with the base angle of attack, α_0, which is reasonable, since the flow becomes increasingly nonlinear for increasing angle of attack. The number of Markov parameters (values of the discrete-time impulse response from OKID used by ERA) is reported.

The inherent time delay between command signal and measured force is identified by choosing the time delay that minimizes the model error for the case of pitching about $\alpha_0 = 0^\circ$. The results are shown in Table 2. Recall from Section 5.1 that the coarse sample time is $\Delta t = 0.1$ convective time units. Since the error is the same for a time delay of $2\Delta t$ and $3\Delta t$, it helps to use other indicators, such as the frequency response or how closely the peaks in $\ddot{\alpha}$ line up with the added-mass peaks in the force measurement. Based on these

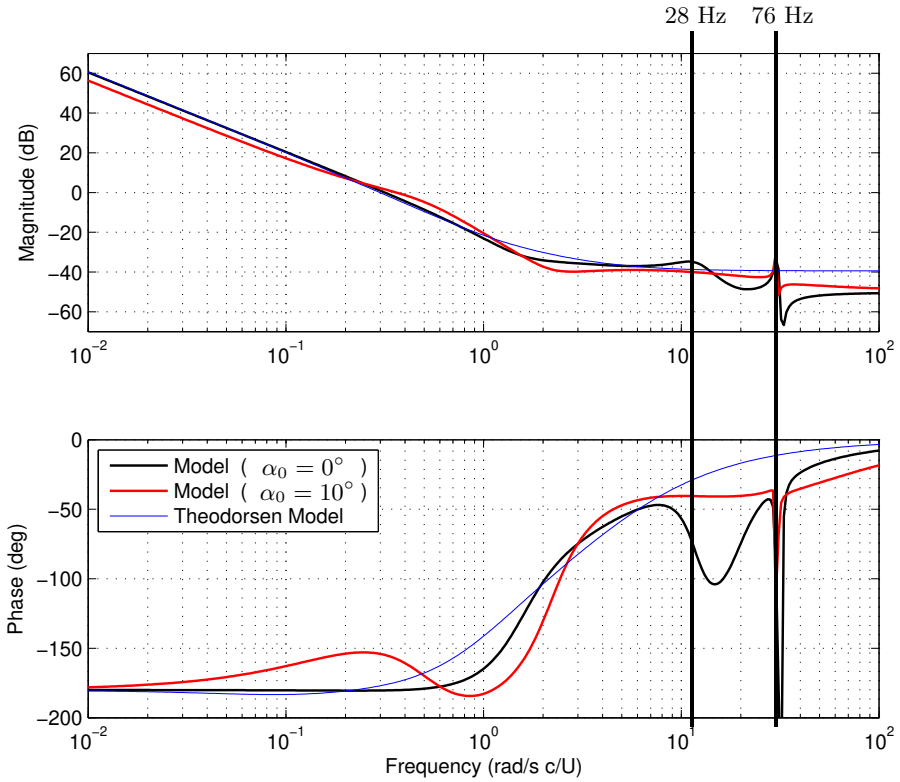

FIGURE 17. Bode plots of pitch models at $\alpha_0 = 0°$ and $\alpha_0 = 10°$. Pitch is about 11% chord.

	Error (Theodorsen)	Error (ERA Model)	Markov parameters	Model order
Pitch, $\alpha_0 = 0°$	0.0604	0.0331	100	7
Pitch, $\alpha_0 = 5°$	0.0752	0.0430	50	5
Pitch, $\alpha_0 = 10°$	0.1279	0.0629	150	5
Plunge, $\alpha_0 = 0°$	0.1414	0.0701	100	5
Plunge, $\alpha_0 = 10°$	0.2028	0.0991	100	5

TABLE 1. Comparison of Theodorsen and ERA model error with wind tunnel measurements for pitch and plunge maneuvers. Error is quantified by computing the standard deviation, from zero mean, of the error signal (measurement minus model).

comparisons, it was determined that the time-delay is $\tau_d = 3\Delta t$ (0.3 convective times). This imposes a fundamental bandwidth limitation for closed-loop feedback control of $1/\tau_d$ rad/s c/U, which is 8.6 Hz in dimensional units. This bandwidth is higher than was reported by Kerstens *et al.* (2011) using leading-edge actuation.

6.4. *Discussion about experimental results*

Reduced-order models for the unsteady lift force have been obtained from wind tunnel measurements of a pitching and plunging airfoil. The wind tunnel is a more challenging test case with the addition of flow disturbances, time-delays, and sensor noise. Addition-

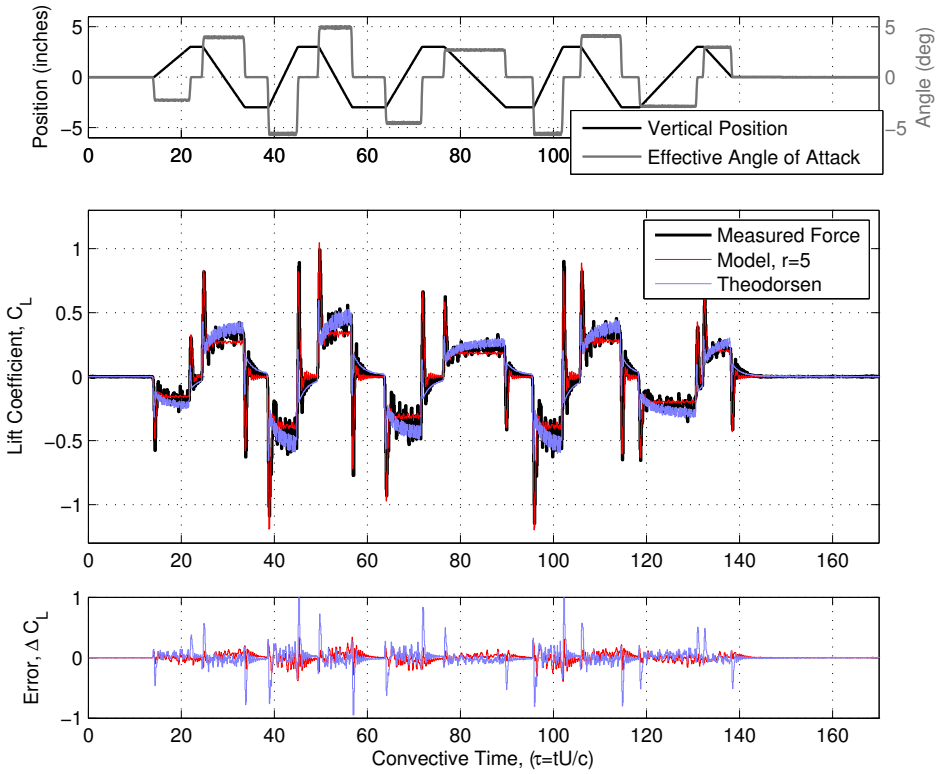

FIGURE 18. Experimental and modeled lift for plunge about a base angle of $\alpha_0 = 0°$.

Model order	7	7	7	7
Time delay (Δt)	1	2	3	4
Error (ERA Model)	0.0359	0.0331	0.0331	0.0727

TABLE 2. Effect of assumed time delay on model error. Model is $\alpha_0 = 0°$ pitch case. 100 Markov parameters are used with $\Delta t = 0.1$ convective time units.

ally, the experiment is performed at a moderate Reynolds number, $Re = 65,000$, with a three-dimensional wing with rounded leading edge, providing a more realistic model of a micro aerial vehicle. The issue of plant disturbance and sensor noise motivates the use of aggressive maneuvers, which excite strong unsteady aerodynamic responses across a range of relevant frequencies. These maneuvers are used in conjunction with the ERA/OKID algorithm to construct pitch and plunge models of the form in Eq. (3.6).

In both pitch and plunge experiments, at $\alpha_0 = 0°$ and $\alpha_0 = 10°$, the reduced-order model outperforms Theodorsen's model. At larger base angle of attack, $\alpha_0 = 10°$, the difference with Theodorsen is more pronounced. At $\alpha_0 = 10°$ both models have larger total error than in the $\alpha_0 = 0°$ case, because of nonlinear flow effects that are not modeled. The fact that the low-order model captures the additional mechanical effects indicates that these methods may be applied more generally to problems in aeroelasticity. There

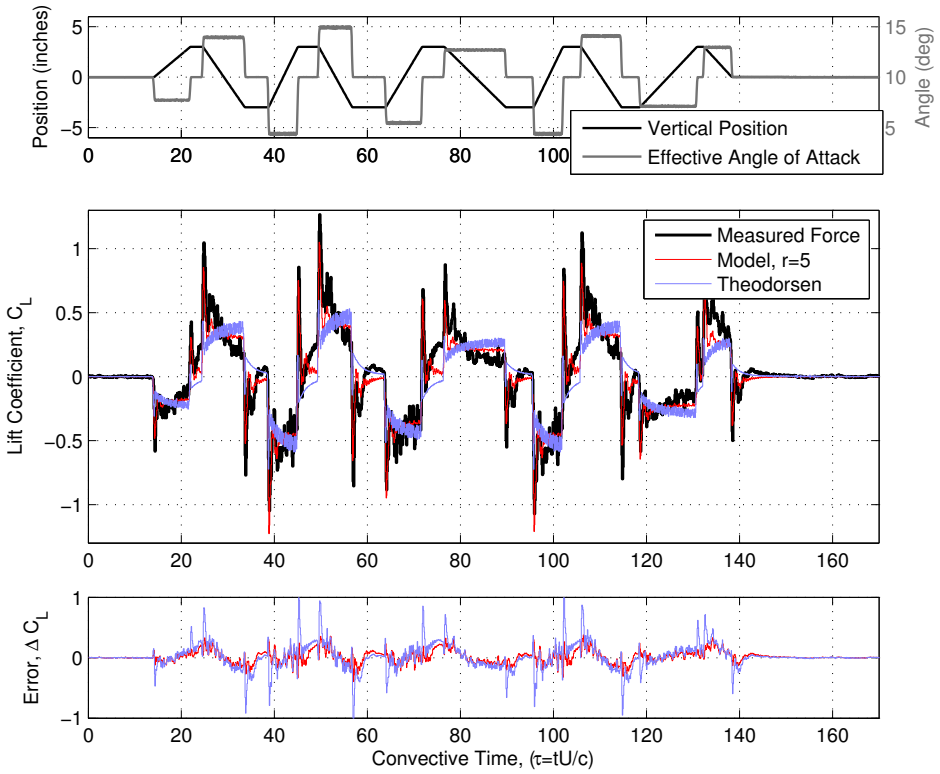

FIGURE 19. Experimental and modeled lift for plunge about a base angle of $\alpha_0 = 10°$.

is also an aerodynamic cushioning effect at $\alpha_0 = 10°$, whereby the mechanical resonance is attenuated and occurs at a slightly higher frequency.

The models based on wind tunnel measurements follow similar trends to those based on simulations. For example, at larger base angle of attack, the model takes longer to equilibrate to steady state, as reflected in the convergence to the quasi-steady asymptote at a lower frequency. Additionally, at $\alpha_0 = 0°$, the data and models exhibit a transient rise to their steady-state values given a step in effective angle of attack, while at $\alpha_0 = 10°$, the data and models exhibit a transient decay to their steady-state values from a larger initial value. In simulations, this is due to leading-edge and trailing-edge separation.

7. Conclusions and discussion

In this work, we have developed reduced-order models, and a flexible modelling procedure, for the unsteady pitching and plunging aerodynamics of two low-Reynolds-number configurations. The first set of results are two-dimensional direct numerical simulations of a flat plate at $Re = 100$. It is shown that for a relatively low order model, with order $r = 7$, the unsteady aerodynamic effects are well captured for all angles of attack up to the Hopf bifurcation angle. The second set of results are based on wind tunnel measurements of a NACA 0006 airfoil at $Re = 65,000$. These experiments motivated the development

of aggressive system identification maneuvers for use with the OKID method, which allows for accurate system identification over a range of frequencies, despite the reduced signal-to-noise ratio experienced in high-reduced-frequency, low-Reynolds-number wind tunnel experiments. The modelling procedure is able to capture the additional dynamics associated with the structural resonance and actuator dynamics in the experiment.

The models presented in this paper provide quantifiable insights into the physics of laminar separation that characterize flows at low Reynolds number. In both the simulated results and the wind tunnel measurements, the low-order models exhibit similar trends as the angle of attack is increased. The quasi-steady model asymptote is pushed to lower frequencies at larger base angle of attack, α_0, consistent with the fact that the boundary layer is becoming more separated and a pair of complex eigenvalues moves toward the imaginary axis in the models. In addition, we observe that poles and zeros of the reduced-order models approach the imaginary axis as the base angle of attack is increased, and at a subcritical angle of attack, some zeros move into the right half plane. This has significant consequences for feedback control; in particular, the introduction of zeros in the right-half complex plane will impose fundamental limitations on the bandwidth that may be achieved with closed-loop feedback control (Kerstens *et al.* 2011). In the experiment, we see an attenuation of the structural resonance at large angle of attack, due to the cushioning effect of the separated boundary layer. In both simulations and experiments, it is observed that there is qualitatively different behavior at low and high base angle of attack for the lift in response to a step-up in angle of attack: at low angle of attack, the lift rises to the steady-state value, whereas at high angle of attack, the lift decreases to the steady-state value from an initial high lift state. This suggests the formation of a leading-edge vortex, followed by trailing-edge separation at large angles of attack, which is confirmed using FTLE visualizations.

An important feature of this study is the determination of flow regimes where these models start to break down. Because the models are reduced-order models of the linearized discrete Navier-Stokes equations with lift output equation, it is expected that they will not be valid for flows that are dominated by nonlinear phenomena, such as vortex shedding or large leading-edge vortex formation. For example, the models are not necessarily valid when the angle of attack, α, or the effective angle of attack, α_e, based on the Strouhal number, exceeds the critical angle of attack at which Hopf bifurcation occurs. As the base angle of attack approaches this critical angle, the radius of validity of the model shrinks. However, it was demonstrated on several large-amplitude maneuvers, in which the flow was massively separated, that the model does surprisingly well, as long as there are large angular or vertical rates associated with the motion, resulting in added-mass.

The models developed here will be particularly useful in the context of active flow control. The low-dimensional state-space form of these models is ideal for use with modern control techniques, such as $\mathcal{H}_2$ and $\mathcal{H}_\infty$ synthesis (Kim & Bewley 2007; Bagheri *et al.* 2009; Ahuja & Rowley 2010). In particular, the authors envision an experimental demonstration of robust lift control that tracks a specified reference lift while rejecting gust disturbances and attenuating sensor noise. As the base angle of attack is increased and zeros enter the right half plane, there will be fundamental limitations on the bandwidth of the closed-loop system. The design of flight controllers for micro aerial vehicles is challenging, since the flight dynamic and fluid dynamic timescales are comparable. The typical control paradigm of inner-loop/outer-loop design will no longer yield robust controllers, and it will become necessary to apply modern control techniques. This is the focus of current work by the authors.

The authors gratefully acknowledge the support for this work from the Air Force Office of Scientific Research grant FA9550-12-1-0075, and by the FAA, under the Joint University Program. We also thank Wes Kerstens, Jeff Eldredge, Michael OL, and the AIAA fluid dynamics technical committee's low-Reynolds-number aerodynamics discussion group.

REFERENCES

Ahuja, S. & Rowley, C. W. 2010 Feedback control of unstable steady states of flow past a flat plate using reduced-order estimators. *Journal of Fluid Mechanics* **645**, 447–478.

Anderson, J. M., Streitlien, K., Barrett, D. S. & Triantafyllou, M. S. 1998 Oscillating foils of high propulsive efficiency. *Journal of Fluid Mechanics* **360**, 41–72.

Bagheri, S., Brandt, L. & Henningson, D. S. 2009 Input-output analysis, model reduction and control of the flat-plate boundary layer. *Journal of Fluid Mechanics* **620**, 263–298.

Birch, J. & Dickinson, M. 2001 Spanwise flow and the attachment of the leading-edge vortex on insect wings. *Nature* **412**, 729–733.

Brennen, C. E. 1982 A review of added mass and fluid inertial forces. *Tech. Rep.* CR 82.010. Naval Civil Engineering Laboratory.

Brunton, S. L. 2012 Unsteady aerodynamic models for agile flight at low Reynolds numbers. PhD thesis, Princeton University.

Brunton, S. L. & Rowley, C. W. 2010 Fast computation of FTLE fields for unsteady flows: a comparison of methods. *Chaos* **20**, 017503.

Brunton, S. L. & Rowley, C. W. 2012 Empirical state-space representations for Theodorsen's lift model. *to appear in Journal of Fluids and Structures* .

Buchholz, J.H.J. & Smits, A. J. 2008 The wake structure and thrust performance of a rigid, low-aspect-ratio pitching panel. *Journal of Fluid Mechanics* **603**, 331–365.

Colonius, T. & Taira, K. 2008 A fast immersed boundary method using a nullspace approach and multi-domain far-field boundary conditions. *Computer Methods in Applied Mechanics and Engineering* **197**, 2131–2146.

Edwards, J. W. 1977 Unsteady aerodynamic modeling and active aeroelastic control. SUDARR 504. Stanford University.

Eldredge, J. D., Wang, C. & OL, M. V. 2009 A computational study of a canonical pitch-up, pitch-down wing maneuver. AIAA Paper 2009-3687, 39th Fluid Dynamics Conference.

Franco, E., Pekarek, D. N., Peng, J. & Dabiri, J. O. 2007 Geometry of unsteady fluid transport during fluid-structure interactions. *Journal of Fluid Mechanics* **589**, 125–145.

Green, M. A., Rowley, C. W. & Haller, G. 2007 Detection of Lagrangian coherent structures in 3D turbulence. *Journal of Fluid Mechanics* **572**, 111–120.

Green, M. A., Rowley, C. W. & Smits, A. J. 2011 The unsteady three-dimensional wake produced by a trapezoidal pitching panel. *Journal of Fluid Mechanics* **685**, 117–145.

Green, M. A. & Smits, A. J. 2008 Effects of three-dimensionality on thrust production by a pitching panel. *Journal of Fluid Mechanics* **615**, 211–220.

Haller, G. 2002 Lagrangian coherent structures from approximate velocity data. *Physics of Fluids* **14** (6), 1851–1861.

Haller, G. 2004 Exact theory of unsteady separation for two-dimensional flows. *Journal of Fluid Mechanics* **512**, 257–311.

Juang, J. N. & Pappa, R. S. 1985 An eigensystem realization algorithm for modal parameter identification and model reduction. *Journal of Guidance, Control, and Dynamics* **8** (5), 620–627.

Juang, J. N., Phan, M., Horta, L. G. & Longman, R. W. 1991 Identification of observer/Kalman filter Markov parameters: Theory and experiments. Technical Memorandum 104069. NASA.

Kaplan, S. M., Altman, A. & Ol, M. 2007 Wake vorticity measurements for low aspect ratio wings at low Reynolds number. *Journal of Aircraft* **44** (1), 241–251.

von Karman, T. & Sears, W. R. 1938 Airfoil theory for non-uniform motion. *Journal Aeronautical Sciences* **5** (10), 379–390.

Kerstens, W., Pfeiffer, J., Williams, D., King, R. & Colonius, T. 2011 Closed-loop

control of lift for longitudinal gust suppression at low Reynolds numbers. *AIAA Journal* **49** (8), 1721–1728.

Kim, J. & Bewley, T. R. 2007 A linear systems approach to flow control. *Annual Review of Fluid Mechanics* **39**, 383–417.

Lesieutre, D. J., Reisenthel, P. H. & Dillenius, M. F. E. 1994 A practical approach for calculating aerodynamic indicial functions with a Navier-Stokes solver. AIAA Paper 94-0059, 32nd Aerospace Sciences Meeting.

Ma, Z., Ahuja, S. & Rowley, C. W. 2011 Reduced order models for control of fluids using the eigensystem realization algorithm. *Theoretical and Computational Fluid Dynamics* **25** (1), 233–247.

Peng, J. & Dabiri, J. O. 2008 The 'upstream wake' of swimming and flying animals and its correlation with propulsive efficiency. *The Journal of Experimental Biology* **211**, 2669–2677.

Pines, D. J. & Bohorquez, F. 2006 Challenges facing future micro-air-vehicle development. *Journal of Aircraft* **43** (2), 290–305.

Pullin, D. I. & Wang, Z. J. 2004 Unsteady forces on an accelerating plate and application to hovering insect flight. *Journal of Fluid Mechanics* **509**, 1–21.

Rowley, C. W. 2005 Model reduction for fluids using balanced proper orthogonal decomposition. *International Journal of Bifurcation and Chaos* **15** (3), 997–1013.

Ruelle, D. & Takens, F. 1971 On the nature of turbulence. *Communications in Mathematical Physics* **20**, 167–192.

Sane, S. P. 2003 The aerodynamics of insect flight. *The Journal of Experimental Biology* **206** (23), 4191–4208.

Shadden, S. C., Katija, K., Rosenfeld, M., Marsden, J. E. & Dabiri, J. O. 2007 Transport and stirring induced by vortex formation. *Journal of Fluid Mechanics* **593**, 315–331.

Shadden, S. C., Lekien, F. & Marsden, J. E. 2005 Definition and properties of Lagrangian coherent structures from finite-time Lyapunov exponents in two-dimensional aperiodic flows. *Physica D* **212**, 271–304.

Surana, A., Grunberg, O. & Haller, G. 2006 Exact theory of three-dimensional flow separation. Part 1. Steady separation. *Journal of Fluid Mechanics* **564**, 57–103.

Taira, K. & Colonius, T. 2007 The immersed boundary method: a projection approach. *Journal of Computational Physics* **225** (2), 2118–2137.

Taira, K. & Colonius, T. 2009 Three-dimensional flows around low-aspect-ratio flat-plate wings at low Reynolds numbers. *Journal of Fluid Mechanics* **623**, 187–207.

Theodorsen, T. 1935 General theory of aerodynamic instability and the mechanism of flutter. *Tech. Rep.* 496. NACA.

Torres, G. E. & Mueller, T. J. 2004 Low-aspect-ratio wing aerodynamics at low Reynolds numbers. *AIAA Journal* **42** (5), 865–873.

Triantafyllou, G. S., Triantafyllou, M. S. & Grosenbaugh, M. A. 1993 Optimal thrust development in oscillating foils with application to fish propulsion. *Journal of Fluids and Structures* **7**, 205–224.

Truong, K. V. & Tobak, M. 1990 Indicial response approach derived from Navier-Stokes equations. Part 1: Time-invariant equilibrium state. Technical Memorandum 102856. NASA.

Videler, J. J., Samhuis, E. J. & Povel, G. D. E. 2004 Leading-edge vortex lifts swifts. *Science* **306**, 1960–1962.

Wagner, H. 1925 Über die Entstehung des dynamischen Auftriebes von Tragflügeln. *Zeitschrift für Angewandte Mathematic und Mechanik* **5** (1), 17–35.

Wang, Z. J. 2005 Dissecting insect flight. *Annual Review of Fluid Mechanics* **37**, 183–210.

Weldon, M., Peacock, T., Jacobs, G. B., Helu, M. & Haller, G. 2008 Experimental and numerical investigation of the kinematic theory of unsteady separation. *Journal of Fluid Mechanics* **611**, 1–11.

Wilson, M. M., Peng, J., Dabiri, J. O. & Eldredge, J. D. 2009 Lagrangian coherent structures in low Reynolds number swimming. *Journal of Physics: Condensed Matter* **21** (20), 204105.

Zbikowski, R. 2002 On aerodynamic modelling of an insect-like flapping wing in hover for micro air vehicles. *Philosophical Transactions of the Royal Society A* **360**, 273–290.